

# The Modulation of Interdecadal Pacific Oscillation and Atlantic Multidecadal Oscillation on winter Eurasian Cold Anomaly via the Ural Blocking Change

**Binhe Luo**

Ocean University of China - Laoshan Campus: Ocean University of China

**Dehai Luo** (✉ [ldh@mail.iap.ac.cn](mailto:ldh@mail.iap.ac.cn))

RCE-TEA, Institute of Atmospheric Physics, Chinese Academy of Science

**Aiguo Dai**

University at Albany State University of New York

**Simmonds Ian**

The University of Melbourne

**Lixin Wu**

Ocean University of China - Laoshan Campus: Ocean University of China

---

## Research Article

**Keywords:** Eurasian cold anomaly (ECA) , Modulation , Interdecadal Pacific Oscillation, Atlantic Multidecadal Oscillation, Ural Blocking Change

**Posted Date:** May 6th, 2021

**DOI:** <https://doi.org/10.21203/rs.3.rs-437125/v1>

**License:**  This work is licensed under a Creative Commons Attribution 4.0 International License.

[Read Full License](#)

---

**Version of Record:** A version of this preprint was published at Climate Dynamics on January 5th, 2022. See the published version at <https://doi.org/10.1007/s00382-021-06119-7>.

1  
2  
3 **The modulation of Interdecadal Pacific Oscillation and Atlantic**  
4 **Multidecadal Oscillation on winter Eurasian cold anomaly via the**  
5 **Ural blocking change**

6  
7  
8 Binhe Luo<sup>a,b</sup>), Dehai Luo<sup>b</sup>), Aiguo Dai<sup>c</sup>), Ian, Simmonds<sup>d</sup>) and Lixin Wu<sup>a</sup>)  
9

10 (a) Key Laboratory of Physical Oceanography/Institute for Advanced Ocean Studies, Ocean  
11 University of China and Qingdao National Laboratory for Marine Science and Technology,  
12 Qingdao, China

13 (b) Key Laboratory of Regional Climate-Environment for Temperate East Asia, Institute of  
14 Atmospheric Physics, Chinese Academy of Sciences, Beijing, China, 100029 and  
15 University of Chinese Academy of Sciences, Beijing, China

16 (c) Department of Atmospheric and Environmental Sciences, University at Albany, SUNY,  
17 Albany, NY 12222, USA

18 (d) School of Earth Sciences, The University of Melbourne, Victoria, Australia

19 *Submitted to Climate Dynamics*

20 Date: 16 April, 2021

21 Corresponding author address: Dr. Dehai Luo, Institute of Atmospheric Physics, Chinese

22 Academy of Science, Beijing, 100029, Email: [ldh@mail.iap.ac.cn](mailto:ldh@mail.iap.ac.cn)

23

24

## Abstract

25

26

27

28

29

30

31

32

Observations revealed distinct interdecadal winter Eurasian cold anomaly (ECA) centered over central Eurasia ( $40^{\circ}$ - $60^{\circ}$ N, $60^{\circ}$ - $120^{\circ}$ E), with a more southwestward extension during 1965-1976 than during 2002-2013. In this paper, Ural blockings (UB) in association with the Interdecadal Pacific Oscillation (IPO) and Atlantic Multi-decadal Oscillation (AMO) are analyzed to explain the ECA's interdecadal change using reanalysis data. It is found that the 1965-1976 winter ECA is associated with the negative-phase IPO (IPO<sup>-</sup>) together with negative-phase AMO (AMO<sup>-</sup>), while the 2002-2013 ECA is related to positive-phase AMO (AMO<sup>+</sup>) concurring with IPO<sup>-</sup>.

33

34

35

36

37

38

39

40

41

42

43

44

The UB mainly related to positive North Atlantic Oscillation is long-lived during IPO<sup>-</sup> and AMO<sup>+</sup> and shows different longitudinal position and movement, but short-lived and retrograde during both IPO<sup>+</sup> and AMO<sup>-</sup>. During IPO<sup>-</sup>, the UB grows rapidly and decays slowly due to weak westerly winds and small meridional potential vorticity gradient ( $PV_y$ ) over North Atlantic mid-high latitudes, and moves westward mainly during its decay stage, causing strong cold anomalies over central Eurasia and its upstream region ( $30^{\circ}$ - $50^{\circ}$ N,  $30^{\circ}$ - $70^{\circ}$ E). Such a slow blocking decay is also seen during AMO<sup>-</sup>. However, during AMO<sup>+</sup> the UB grows slowly, decays rapidly and shows eastward movement due to strong westerly winds and large  $PV_y$  over North Atlantic high latitudes, causing strong cold anomalies over central Eurasia and its downstream region ( $30^{\circ}$ - $50^{\circ}$ N,  $90^{\circ}$ - $130^{\circ}$ E). Through these UB-induced sub-seasonal changes, the interdecadal IPO<sup>-</sup>, AMO<sup>-</sup> and AMO<sup>+</sup> help explain the variation of the winter-mean ECA from 1965-1976 to 2002-2013.

## 45 **1. Introduction**

46 Earth's warming rate slowed down noticeably during 2000-2013, which is often referred to  
47 as the recent global warming hiatus (Kaufmann et al. 2011; Karl et al. 2015). The physical  
48 cause of the global warming hiatus has been a focus of climate research in recent years  
49 (Trenberth and Fasullo, 2013; Kosaka and Xie 2013; Chen and Tung, 2014; Trenberth, 2015;  
50 Marotzke and Forster 2015; Wei et al. 2015; Meehl et al. 2016; Huang et al. 2017). Many  
51 studies have revealed that the recent warming hiatus was mainly caused by internal  
52 multi-decadal variability in Pacific and Atlantic sea surface temperatures (SSTs), primarily  
53 associated with the Interdecadal Pacific Oscillation (IPO) (Meehl et al. 2013, 2016; Dai et al.  
54 2015) and the Atlantic Multidecadal Oscillation (AMO) (Dai et al. 2015; Steinman et al. 2015).  
55 Furthermore, some studies indicated that the hiatus was associated with the anomalously cold  
56 surface air temperatures over Eurasia seen mainly in winter (Cohen et al. 2012; Li et al. 2015;  
57 Luo et al. 2016; Yao et al. 2017; Huang et al. 2017; Deser et al. 2017). In particular, Deser et al.  
58 (2017) found that the Eurasian cold anomaly (ECA) may account for 71% of the recent  
59 slowdown in winter global warming rate during 2000-2013. The winter ECA also occurred  
60 during 1965-1976 (Wei et al. 2015; Huang et al. 2017), and the winter ECA's interdecadal  
61 variation is found to be associated with the North Atlantic interdecadal variability (Sung et al.  
62 2018). Thus, it is likely that the IPO and AMO may have contributed to the decadal winter  
63 ECAs, including the recent warming hiatus.

64 Previous studies have established a connection between the interdecadal variability of  
65 Northern Hemisphere (NH) or global winter air temperatures and the IPO and AMO from the

66 statistical and dynamical perspectives (Wyatt et al. 2012; Dai et al. 2015; Steinman et al. 2015;  
67 Dong and Dai 2015; Sung et al. 2018). However, it is unclear how and whether the IPO and  
68 AMO could influence winter ECA through their modulation of the Ural blocking (UB), a  
69 blocking anticyclone over the Ural Mountains around 60°E and 50°-70°N on a timescale of  
70 10-20 days, as the winter ECA is closely related to the presence of UB (Luo et al. 2016a-b; Yao  
71 et al. 2017). In particular, we do not know why the spatial distribution of the winter ECA  
72 exhibits a large change from 1965-1976 to 2002-2013, and whether and how the spatial pattern  
73 of the winter ECA depends on the phases of AMO and IPO or their combinations. While the  
74 UB frequency is linked to sea ice loss in Barents-Kara Seas (BKS) (Mori et al. 2014; Luo et al.  
75 2017a; Li et al. 2021), the warm Arctic-cold Siberia (WACS) pattern in winter is associated  
76 with the presence of UB (Luo et al. 2016a) and its trend during 1990-2014 is related to  
77 increased UB frequency (Mori et al. 2014; Tyrllis et al. 2020; Kim et al. 2021). However, UB's  
78 longitudinal location, movement and persistence are more important for the occurrence region  
79 and strength of the sub-seasonal ECA over central Eurasia than the strength of blocking itself  
80 (Yao et al. 2017). In contrast, the European blocking and Atlantic blocking are not important  
81 for the cold anomaly over central Eurasia (B. Luo et al. 2019), while the interdecadal  
82 variability of Euro-Atlantic blocking is also related to AMO (Rimbu et al. 2014). Furthermore,  
83 Luo et al. (2017b) linked the spatial shape of UB to the AMO. As the winter-mean ECA is  
84 derived from the sub-seasonal ECA, we hypothesize that the UB-induced changes in  
85 sub-seasonal ECAs may play an important role in causing the recent winter decadal ECA.  
86 Nevertheless, what causes the UB in its position, movement and evolution and the sub-seasonal

87 ECA to vary on decadal time scale is unclear. In particular, the different roles of the IPO and  
88 AMO in causing the decadal variations in the UBs and associated sub-seasonal cold anomalies  
89 over central Eurasia have not been examined.

90 While Luo et al. (2017b) found that a positive AMO phase ( $AMO^+$ ) favors persistent  
91 northwest-southeast-oriented UB patterns that enhance the sub-seasonal ECAs, they did not  
92 explain why a winter ECA occurred during 1965-1976 and had a large difference from the  
93 2002-2013 ECA. Moreover, how UB's position, movement and evolution (i.e., growth and  
94 decay) change with the IPO and AMO, and how such UB changes influence the sub-seasonal  
95 ECA are not explored in Luo et al. (2017b) or any other studies. Here, we investigate the  
96 different behavior of the UB under different phases of IPO or AMO and offer a synoptic  
97 explanation from a blocking perspective for why the spatial pattern of the winter ECA shows a  
98 distinct change from 1965-1976 to 2002-2013. We refer to this winter ECA change from  
99 1965-1976 to 2002-2013 as the decadal change of ECA in this paper. Because the IPO and  
100 AMO are multidecadal modes, they do not directly excite UB events which have a sub-seasonal  
101 time scale of 10-20 days. Instead, it can induce interdecadal temperature anomalies and the  
102 change in atmospheric background condition and then influence the UB. Thus, we hypothesize  
103 that the phase of IPO or AMO can contribute to the change of the winter ECA from 1965-1976  
104 to 2002-2013 through interdecadal temperature anomalies and their interdecadal modulation of  
105 UB's position, movement, evolution and persistence. We are particularly interested to  
106 investigate whether there are different behaviors of the UBs associated with IPO and AMO,  
107 and their different modulations of the UB and the associated sub-seasonal ECA. It appears that

108 the role of the UB's interdecadal change induced by IPO and AMO in the winter ECA change  
109 is more important than interdecadal cold anomalies associated with IPO and AMO themselves.  
110 These results help explain the change in the spatial pattern of the winter ECA from 1965-1976  
111 to 2002-2013, which are not reported in previous studies (e.g., Luo et al. 2017; Sung et al. 2018;  
112 B. Luo et al. 2019).

113 This paper is organized as follows: In section 2, we describe the data and method. Section  
114 3 describes the connections of the ECA during 1965-1976 and 2002-2013 to changes in the UB  
115 events. In section 4, we examine how the phase of IPO or AMO modulates the sub-seasonal  
116 ECA through changing the position, movement, persistence and evolution of UB events.  
117 Section 5 examines the physical processes through which the IPO or AMO modulates the UBs.  
118 A summary and conclusions are presented in section 6.

## 119 **2.Data and method**

120 We used the daily data on a  $2.5^\circ \times 2.5^\circ$  grid for winter (December, January and February,  
121 DJF) during the period from December 1950/February 1951 to December 2017/February 2018  
122 (1950-2017, hereafter) taken from National Centers for Environmental Prediction-National  
123 Center for Atmospheric Research (NCEP-NCAR) reanalysis (Kalnay et al. 1996). They include  
124 sea level pressure (SLP), surface air temperature (SAT), 500-hPa geopotential height (Z500)  
125 and zonal wind (U500). All the daily data were converted into anomalies by removing the  
126 1950-2017 mean for each calendar day, and then detrended prior to analyses. We also used the  
127 winter monthly sea ice concentration (SIC) and sea surface temperature (SST) data on a  $1^\circ \times 1^\circ$   
128 grid during 1950-2017 from the HadISST1 obtained from the Hadley Centre (Rayner et al.

129 2003).

130 There are many ways to define the Interdecadal Pacific Oscillation (IPO) (Dai 2013; Dong  
131 et al. 2018; Hua et al. 2018, 2019). As in van Oldenborgh et al. (2009), the winter IPO is  
132 defined as the principal component (PC) of the first EOF of detrended, 4-year moving averaged  
133 DJF-mean SST from HadISST1 over 50°S-50°N, 100°E-70°W. Here, we used the winter IPO  
134 index obtained from the Koninklijk Nederlands Meteorologisch Instituut (KNMI) Climate  
135 Explorer. Following Trenberth and Shea (2006), we used the DJF-mean SST anomalies from  
136 HadISST1 averaged over 0°-60°N, 0°-80°W minus the DJF-mean SST anomalies averaged over  
137 the global oceans from 60°S-60°N as the Atlantic Multidecadal Oscillation (AMO) index,  
138 which was also obtained from the KNMI Climate Explorer. Results are similar if the AMO  
139 index from Kaplan et al. (1998) is used. Below, we will use the 9-year smoothed IPO and AMO  
140 indices to examine the modulation of the IPO and AMO on UB and associated sub-seasonal  
141 ECA to explain the change of the winter ECA from 1965-1976 to 2002-2013.

142 Here, we define a positive (negative) phase IPO or IPO<sup>+</sup> (IPO<sup>-</sup>) as the year with positive  
143 (negative) values above (below) 0.5 (-0.5) standard deviations (STDs) for the 9-year smoothed  
144 DJF-mean IPO index. The positive (negative) phase AMO or AMO<sup>+</sup> (AMO<sup>-</sup>) is similarly  
145 defined using the 9-year smoothed DJF-mean AMO index. To guarantee that there are enough  
146 the sample size of the IPO/AMO combination winters, we used a positive or negative STD to  
147 define the IPO/AMO combination. As in Huang et al. (2019), an IPO<sup>-</sup> and AMO<sup>-</sup> (or  
148 IPO<sup>-</sup>/AMO<sup>-</sup>) combination winter is defined if their normalized indices are negative below 0  
149 STD, whereas an IPO<sup>-</sup> and AMO<sup>+</sup> (or IPO<sup>-</sup>/AMO<sup>+</sup>) combination winter is defined if the 9-year

150 smoothed IPO (AMO) index is negative below 0 STD (positive above 0 STD). The other  
151 combination winters are similarly defined. The results based on the 0.5 STD definition are  
152 similar and given in the supplementary file.

153 To identify UB events in the Ural Mountains region around 60°E, the one-dimensional (1D)  
154 blocking index of Tibaldi and Molteni (1990, TM hereafter) is used to calculate UB events over  
155 the region 40°-80°E. The TM index is based on the reversal of the meridional gradient of Z500:  
156 
$$\text{GHGN} = \frac{Z500(\phi_N) - Z500(\phi_o)}{\phi_N - \phi_o} \quad \text{and} \quad \text{GHGS} = \frac{Z500(\phi_o) - Z500(\phi_S)}{\phi_o - \phi_S}$$
 at three given latitudes  
157  $\phi_N = 80^\circ N + \Delta$ ,  $\phi_o = 60^\circ N + \Delta$ ,  $\phi_S = 40^\circ N + \Delta$  and  $\Delta = -5^\circ, 0^\circ, 5^\circ$ . A blocking event is  
158 defined to have taken place in a given region if both GHGS > 0 and GHGN < -10 gpm (deg  
159 lat)<sup>-1</sup> persist at least three consecutive days and are satisfied for at least one choice of  $\Delta$ . At the  
160 same time, the duration of the UB is estimated as the consecutive days with the daily Z500  
161 anomaly averaged over the blocking latitude band (50°-70°N) exceeding a threshold of 80 gpm,  
162 and used to represent the local persistence time of the UB in the Ural region as in Luo et al.  
163 (2018a). The change speed of the daily zonal location of the maximum anticyclonic anomaly  
164 averaged over 50°-70°N is defined as the daily phase speed of UB, whereas its time-mean value  
165 averaged over the blocking duration confined in the Ural region is defined as the mean  
166 movement speed of the UB. In our composite of UB events, the peak day of the GHGS is  
167 defined as lag 0 day of the UB (B. Luo et al. 2017b).

168 Diao et al. (2006) evaluated the different blocking indices in identifying the blocking action  
169 in the NH and demonstrated that the 1D TM index is an appropriate metric for identifying  
170 blocking events over the Ural region. We compared different blocking indices (e.g., the 1D TM

171 index and the PV- $\theta$  index of Masato et al. 2013a-b and Woollings et al. 2008), and found that  
172 the UB events and their durations are not very sensitive to the choice of the blocking index  
173 (Luo et al. 2018a, Tyrlis et al. 2020, 2021). Thus, in this paper we use only the 1D TM index to  
174 identify UB events.

175 Our daily NAO index was taken from the NOAA /Climate Prediction Center. We also  
176 define a NAO<sup>+</sup> (NAO<sup>-</sup>) event to have taken place if the daily NAO index is equal to or above  
177 0.5 (below -0.5) STDs and persists for at least three consecutive days. Other daily events are  
178 defined as neutral NAO (NAO<sup>o</sup>) events if it is neither an individual NAO<sup>+</sup> nor NAO<sup>-</sup> event. The  
179 UB event can be defined as being related to the NAO<sup>+</sup> (NAO<sup>-</sup>) event and referred to as the  
180 UB-NAO<sup>+</sup> (UB-NAO<sup>-</sup>) event if the peak of the GHGS associated with the UB occurs within the  
181 life cycle of the NAO<sup>+</sup> (NAO<sup>-</sup>) event (e.g., B. Luo et al. 2017). The UB event with NAO<sup>o</sup> is  
182 referred to as the UB-NAO<sup>o</sup> event.

183 We used the two-sided Student t-test for determining the statistical significance of the  
184 anomaly field at each grid or the difference between two types of anomaly fields, but the Monte  
185 Carlo test (using 5000 simulations generated by repeated random sampling) for the statistical  
186 significance of the difference between two time series or between two duration lengths. Both  
187 tests are conducted at the  $p < 0.05$  level. These methods are described in Wilks (2011).

188 As demonstrated theoretically by Luo et al. (2019b) and Zhang and Luo (2020), the  
189 magnitude of the meridional potential vorticity (PV) gradient (PV<sub>y</sub>) is a key factor influencing  
190 the behavior (duration, movement and evolution) of atmospheric blocking. The

191 non-dimensional PV<sub>y</sub> at 500 hPa is defined as  $PV_y = \beta - \frac{\partial U_{500}}{\partial y} + FU_{500}$  ( $F \approx 1$  for a

192 barotropic atmosphere and  $\beta$  is the non-dimensional meridional gradient of the Coriolis  
193 parameter  $f$ ), and  $U_{500}$  is the basic zonal wind at 500 hPa, which can be directly calculated  
194 using non-dimensional DJF-mean 500-hPa zonal wind fields for blocking events excluded.  
195 When  $PV_y$  is small in the blocking region, atmospheric blocking has weak energy dispersion  
196 and strong nonlinearity such that it can have a long lifetime (Luo et al. 2019b). The strength of  
197 the upstream westerly wind or  $PV_y$  is important for whether the blocking shows different  
198 evolution (growth and decay) (Zhang and Luo 2020) and movement (Yao et al. 2017). When  
199 the upstream westerly wind or  $PV_y$  is weak, the atmospheric blocking exhibits rapid growth  
200 and slow decay. The reverse is seen for a strong upstream westerly wind or a large upstream  
201  $PV_y$  (Zhang and Luo 2020). Below, we will use these insights to explain why the IPO or AMO  
202 can influence the persistence, movement and evolution of the UB and their different impacts on  
203 Eurasian temperatures by examining the changes in DJF-mean westerly wind and  $PV_y$  related  
204 to the phase of IPO or AMO.

### 205 **3. Decadal Eurasian cold anomalies and their linkage to UB events**

#### 206 *a. Role of UB in the decadal Eurasian cold anomalies*

207 Dai et al. (2015) and Deser et al. (2017) have noted that the recent global warming hiatus  
208 was related to the decadal winter cold anomalies over Eurasia located mainly south of 60°N.  
209 Thus, it is useful to examine the physical cause of the decadal variability of the Eurasian cold  
210 anomaly south of 60°N. Figure 1a shows the time series of DJF-mean SAT anomalies averaged  
211 over central Eurasia (40°-60°N, 60°-120°E) from December 1950 to February 2018, with the  
212 DJF-mean SLP and SAT anomaly patterns during 1965-1976 and 2002-2013 shown in Figs.

213 1b-d. It is clear that winter cold anomalies occurred mainly during 1965-1976 (Fig. 1b) and  
214 2002-2013 (Fig.1c), but the cold anomaly is stronger and extends more to west and south of  
215 central Eurasia during 1965-1976 than during 2002-2013. This can be clearly seen from their  
216 difference field (Fig.1d) with the SAT difference in the upstream region (30°-70°E) of Siberia  
217 being statistically significant ( $p<0.05$ ). The cause of such an interdecadal change has not been  
218 examined in previous studies. However, when the UB events (i.e., the blocking days from lag  
219 -10 to 10 days with lag 0 denoting the peak day of the UB) and associated sub-seasonal ECAs  
220 are removed from the DJF-mean SLP or Z500 and SAT fields, the winter ECAs become much  
221 weaker in the south of 60°N for both 1965-1976 (Fig. 1e) and 2002-2013 (Fig. 1f) than those  
222 with UB events (Figs. 1b-c). For this case, the significant cold anomaly is mainly located in the  
223 north of 60°N (Figs. 1e-f). The difference of the DJF-mean SLP and SAT anomalies between  
224 Figs. 1b and 1e shows that the presence of the UB is crucial for the 1965-1976 winter ECA (Fig.  
225 1g). But the difference between Figs. 1c and 1f indicates that the UB is also important for the  
226 2002-2013 winter ECA (not shown). Thus, the above results suggest that the UB plays an  
227 important role in causing the winter ECA over central Eurasia and its decadal change from  
228 1965-1976 to 2002-2013 through the generation of sub-seasonal ECAs.

229 It should be noted that the warm anomaly over central Eurasia during 1980-2000 is related  
230 to more NAO<sup>+</sup> events without UB (2.54 events per winter), compared to the lower frequencies  
231 during 1965-1976 (1.25 events per winter) and 2002-2013 (1.83 events per winter). Because  
232 the NAO<sup>+</sup> and NAO<sup>-</sup> events without UB cannot directly produce cold anomalies over central  
233 Eurasia (Fig. S1 in the supplementary file), below we don't discuss the roles of NAO<sup>+</sup> and

234 NAO events without UB, but instead we examine the role of the UB in the sub-seasonal ECA.

235 Figs. 2a-d show the time series of the number of UB events in winter and the time-mean  
236 composite daily SLP and SAT anomalies averaged during the UB events from lag -10 to 10  
237 days in three decadal epochs: 1965-1976, 1980-2000 and 2002-2013. Correspondingly, the  
238 time-longitude evolutions of composite daily Z500 anomalies averaged over 50°-70°N during  
239 the UB life cycle are shown in Figs. 2e-g for 1965-1976, 1980-2000 and 2002-2013. It is found  
240 from Fig. 2a that there are 29, 30 and 21 UB events (or 2.42, 1.43, and 1.75 UB events per  
241 winter) during 1965-1976, 1980-2000, and 2002-2013, respectively. An increased trend of the  
242 UB events is seen during 2000-2013, which also corresponds to an increased trend of the UB  
243 duration (Luo et al. 2018, their Fig. 2). This is consistent with the result of Tyrlis et al. (2020,  
244 their Fig. 2) using the PV- $\theta$  index, who found that during 1990-2014 the trend in the warm  
245 Arctic-cold Siberia (WACS) pattern is related to the increasing winter UB frequency (the event  
246 frequency times duration). Because the difference of the UB event frequency between  
247 1965-1976 and 2002-2013 is not statistically significant (at the 90% confidence level based on  
248 a Monte-Carlo test), the change of the winter UB event frequency cannot explain the Eurasian  
249 SAT change from 1965-1976 to 2002-2013.

250 To understand the mechanisms behind this change, Figs. 2b-d suggest that while the strong  
251 Eurasian cold anomalies mainly over central Eurasia during both 1965-1976 and 2002-2013  
252 (Figs. 2b, d) are associated with long-lived UB events (Figs. 2e, g), the sub-seasonal ECA  
253 extends more southwest and covers a wider region in 1965-1976 (Fig. 2b) than in 2002-2013  
254 (Fig. 2d) because UB is located in the upstream side of the Ural region during 1965-1976

255 (Fig.2b). Such a sub-seasonal ECA difference is related to the difference of the UB in  
256 longitudinal position, movement and evolution between 1965-1976 and 2002-2013. The UB  
257 moves westward especially during the decaying phase and grows rapidly but decays slowly  
258 during 1965-1976 (Fig. 2e), whereas it moves eastward and grows slowly but decays rapidly  
259 during 2002-2013 (Fig. 2g). Thus, it is inferred that the sub-seasonal ECA with an enhanced  
260 upstream (downstream) cold anomaly during 1965-1976 (2002-2013) is likely related to the  
261 westward movement, rapid growth and slow decay (eastward movement, slow growth and  
262 rapid decay) of long-lived UBs (Figs. 2e, g). As the UB is displaced westward during  
263 1965-1976, the cold Arctic air can reach farther west and south of central Eurasia through the  
264 cold temperature advection associated with low-level winds (Fig. S2a) (Yao et al. 2017) and  
265 induce a strong upstream cold anomaly (Figs. 2b, e). In contrast, strong cold anomalies are  
266 easily seen over central and eastern Asia during 2002-2013 (Fig. 2d) because of the eastward  
267 shift of the cold temperature advection (Fig. S2c) related to the eastward movement of UB  
268 (Figs. 2g). Moreover, because the UBs have a shorter duration and move rapidly westward  
269 during 1980-2000 (Fig. 2f), the Eurasian warm anomaly during 1980-2000 is also related to  
270 short-lived and rapidly retrograde UB events during this period.

271 We note here that we do not investigate the changes of Eurasian air temperatures from  
272 1965-1976 to 1980-2000 or from 1980-2000 to 2002-2013, as our emphasis is on the  
273 exploration of the physical cause of the interdecadal change of the winter ECA from 1965-1976  
274 to 2002-2013. The calculation shows that the UB has a longer duration of about 9 days (11 days)  
275 over 40°-80°E with a movement speed of -1.4 m/s (1.6 m/s) during 1965-1976 (2002-2013)

276 (Figs. 2e, g) than that of about 7 days with a large retrogression speed of -2.2 m/s during  
277 1980-2000 (Fig. 2f). While the UB's duration difference between 1965-1976 and 2002-2013 is  
278 not statistically significant for a Monte-Carlo test, the UB shows opposite movement and  
279 evolution (growth and decay) between the two periods. Thus, the difference of the winter ECA  
280 spatial patterns between 1965-1976 (Fig. 1b) and 2002-2013 (Fig. 1c) is mainly related to the  
281 different longitudinal position, movement and evolution of long-lived UBs in the two periods  
282 (Figs. 2e, g). These results are not noted in previous studies (Luo et al. 2017b and B. Luo et al.  
283 2019).

284 Here, we further examine whether the change of the UB-related sub-seasonal ECA from  
285 1965-1976 to 2002-2013 is similar to the 1965-1976 minus 2002-2013 winter ECA difference  
286 (Fig. 1d) and whether such a change is mainly related to the interdecadal variation of the  
287 UB-NAO<sup>+</sup> events because most of the UB events are related to NAO<sup>+</sup> (Luo et al. 2016b). Our  
288 calculation reveals that there are 67 UB-NAO<sup>+</sup> (53%) events out of the 126 UB events, but 30  
289 UB-NAO<sup>-</sup> (24%) events and 29 UB-NAO<sup>o</sup> (23%) events during 1950-2017. On average,  
290 UB-NAO<sup>+</sup> events (1.17 and 1.08 cases per winter) during 1965-1976 and 2002-2013 are more  
291 frequent than UB-NAO<sup>-</sup> events (0.67 and 0.42 cases per winter) and UB-NAO<sup>o</sup> events (0.58  
292 and 0.22 cases per winter). Figs. 3a-d show the horizontal fields of time-mean composite daily  
293 Z500 and SAT anomalies averaged from lag-10 to 10 days of UB and UB-NAO<sup>+</sup> events during  
294 1950-2017 and their differences between 1965-1976 and 2002-2013. It is found that the spatial  
295 pattern of the UB-induced cold anomaly for UB-NAO<sup>+</sup> events (Fig. 3b) is similar to that for all  
296 UB events (Fig.3a), although UB-NAO<sup>-</sup> and UB-NAO<sup>o</sup> events influence the cold anomalies

297 over central Eurasia during 1965-1976 and 2002-2013 (not shown). The difference of the  
298 UB-induced sub-seasonal cold anomaly between 1965-1976 and 2002-2013 (Fig.3c) also  
299 resembles the DJF-mean SAT difference between the two periods (Fig. 1d), which is mainly  
300 related to the change of UB-NAO<sup>+</sup> events from 1965-1976 to 2002-2013 (Fig. 3d) because the  
301 UB with NAO<sup>+</sup> (Figs. 3e, f) shows similar behaviors in persistence, movement and evolution to  
302 those of all UB events (Figs. 2e, g). Thus, we do not classify UB events in terms of the phase of  
303 NAO in our following discussions. Instead, we examine the effects of background conditions  
304 associated with AMO and IPO on the UB and associated cold anomaly as well as their changes  
305 from 1965-1976 to 2002-2013 in the next sections.

#### 306 **4. Interdecadal variations of UB events and associated sub-seasonal cold anomalies and** 307 **their linkage to IPO and AMO**

##### 308 *a. Interdecadal SST modes and their linkages to IPO and AMO*

309 Figures 4a-b show the time series of normalized DJF-mean IPO and AMO indices during  
310 1950-2017. In addition, we show the DJF-mean SST anomalies averaged over 1965-1976 and  
311 2002-2013 in Figs. 4c-d, whereas the regressed DJF-mean SST anomalies onto the 9-year  
312 smoothed IPO and AMO indices are shown in Figs. 4e-f. It is shown that the winter IPO  
313 experienced a positive phase (IPO<sup>+</sup>) during 1960-1968, 1979-1998 and 2015-2017; but a  
314 negative phase (IPO<sup>-</sup>) during 1950-1959, 1960-1978 and 2000-2014 (Fig. 4a). The winter AMO  
315 had a positive phase (AMO<sup>+</sup>) during 1950-1960 and 1996-2017; but a negative phase (AMO<sup>-</sup>)  
316 during 1960-1995 (Fig. 4b). Our calculation also revealed that there are 16 IPO<sup>-</sup> and 19 IPO<sup>+</sup> as  
317 well as 22 AMO<sup>-</sup> and 18 AMO<sup>+</sup> winters based on the 0.5 STD definition of the 9-year

318 smoothed IPO and AMO indices during 1950-2017.

319 Clearly, the SST anomaly patterns resemble those for IPO<sup>-</sup> and AMO<sup>-</sup> during 1965-1976  
320 (Fig. 4c), but for IPO<sup>-</sup> and AMO<sup>+</sup> during 2002-2013 (Fig. 4d). The regressed SST anomalies  
321 show that while the IPO<sup>-</sup> mode corresponds to a weak AMO<sup>+</sup> SST anomaly over North Atlantic  
322 (Fig. 4e), the AMO<sup>+</sup> mode can correspond to an IPO<sup>-</sup> SST anomaly over the Pacific (Fig. 4f),  
323 although weaker than that of the IPO<sup>-</sup> mode (Fig. 4e). Because the relationship between IPO  
324 and AMO has been discussed in detail in other studies (e.g., Zhang and Delworth 2007; Meehl  
325 et al. 2021), examining their mutual relationship is beyond the scope of our present study. A  
326 comparison between Figs. 4e-f and Figs. 4c-d leads us to infer that the 1965-1976 ECA is likely  
327 related to the IPO<sup>-</sup> and AMO<sup>-</sup> modes or their combination, whereas the 2002-2013 ECA is  
328 related to the IPO<sup>-</sup> and AMO<sup>+</sup> modes or their combination.

329 *b. Modulation of IPO and AMO on the UB and sub-seasonal cold anomalies*

330 In this subsection, a composite of DJF-mean Z500 and SAT anomalies with and without UB  
331 events in IPO<sup>-</sup>, AMO<sup>-</sup> and AMO<sup>+</sup> winters is first shown in Fig. 5 to help us consider whether  
332 IPO and AMO without UB contribute to the winter ECAs. Figure 5a shows that the IPO<sup>-</sup> with  
333 UB corresponds to a strong winter cold anomaly over central Eurasia. But when UB events are  
334 excluded from the IPO<sup>-</sup> winters, no strong cold anomaly appears over central Eurasia, but  
335 mainly north of 60°N for IPO<sup>-</sup> (Fig. 5b). For AMO<sup>+</sup> there is no strong ECA for both cases with  
336 and without UB (Figs. 5c-d). For AMO<sup>-</sup> a relatively strong cold anomaly appears in the  
337 upstream and south sides of central Eurasia (Fig. 5e), but almost disappears when the UB  
338 events are excluded (Fig. 5f). Thus, AMO<sup>-</sup> without UB cannot produce interdecadal cold

339 anomalies in the south of 60°N over Eurasia, but can correspond to strong high latitude cold  
340 anomalies over Eurasia (north of 60° N). Similar results are found using the zero (instead of  
341  $\pm 0.5$ ) threshold for defining the IPO and AMO phases (Fig. S3). Thus, although AMO<sup>+</sup> or  
342 AMO<sup>-</sup> cannot produce strong cold anomaly over central Eurasia south of 60°N as seen in  
343 observations (Fig. 1b-c) if the UB is absent, IPO<sup>-</sup> without UB cannot contribute to the  
344 interdecadal cold anomalies over central Eurasia (Fig.5b). These results suggest that UB events  
345 modulated by IPO<sup>-</sup>, AMO<sup>-</sup> and AMO<sup>+</sup> play an important role in the winter cold anomaly over  
346 central Eurasia. By comparison, the interdecadal cold anomaly during IPO<sup>-</sup> without UB in the  
347 winter ECA is weak only with a small area of cold anomaly in the downstream side of 120°E.

348 Figure 6 shows the time series of winter UB events for IPO<sup>-</sup>, IPO<sup>+</sup>, AMO<sup>-</sup> and AMO<sup>+</sup>.  
349 There are 36 (34) total events or 2.25 (1.79) UB events per winter during IPO<sup>-</sup> (IPO<sup>+</sup>) (Figs.  
350 6a-b), but 43 (33) total events or 1.95 (1.83) UB events per winter during AMO<sup>-</sup> (AMO<sup>+</sup>) (Figs.  
351 6c-d). Thus, the UB event number does not vary greatly among the IPO<sup>-</sup>, IPO<sup>+</sup>, AMO<sup>-</sup> and  
352 AMO<sup>+</sup> phases. This is expected because the UB (mostly UB-NAO<sup>+</sup>) events are mainly excited  
353 by the decay of the NAO<sup>+</sup> through energy dispersion or wave train propagation (Luo et al.  
354 2016b, 2018b), which does not strongly depend on the phase of IPO or AMO. However, the  
355 IPO or AMO can modulate the decadal background condition and significantly affect the  
356 longitudinal position, duration, movement and evolution of the UB events.

357 To understand how the phase of IPO or AMO influences the behaviors of UB and  
358 associated sub-seasonal ECA, we show the time-mean composites of daily Z500 and SAT  
359 anomalies averaged from lag -10 to 10 days of the UB events and time-longitude evolutions of

360 the composite daily Z500 anomalies averaged over 50°-70°N in Figs. 7-8 for the two phases of  
361 IPO and AMO, respectively. It is seen that a strong sub-seasonal ECA appears over central  
362 Eurasia and its upstream side during the UB events for IPO<sup>-</sup> (Fig. 6a) as the UB has a strong  
363 negative height anomaly at 60°E and its east side, a long duration of about 9.5 days with rapid  
364 growth and persistent slow decay, and a small westward speed of about -0.2 m/s in the Ural  
365 region mainly occurring after lag 3 (Fig. 7d). The UB is mainly located in the upstream side of  
366 Ural region. In contrast, a weak ECA is seen for IPO<sup>+</sup> (Fig. 7b) as the UB has a very weak  
367 negative Z500 anomaly, a short lifespan (~7 days), and a large retrogression speed of about -2.0  
368 m/s but without rapid growth and persistent slow decay (Fig. 7e). Thus, the UB has a larger  
369 contribution to the cold anomaly upstream of central Eurasia during IPO<sup>-</sup> than during IPO<sup>+</sup>  
370 because of the westward displacement and long lifetime of UB and its rapid growth and slow  
371 decay during IPO<sup>-</sup>.

372 A relatively strong cold anomaly is seen over central Eurasia and its upstream side during  
373 the UB events for AMO<sup>-</sup> (Fig. 8a) as the UB has a negative height anomaly around 40°-120°E,  
374 a relatively short duration (~7 days), a westward movement of about -1.0 m/s (Fig. 8d) and a  
375 distinct slow decay but weaker than that during IPO<sup>-</sup> (Fig.7d). But the UB corresponds to a  
376 strong cold anomaly over central Eurasia and its downstream side for AMO<sup>+</sup> (Fig. 8b) because  
377 it shows slow growth and rapid decay with a duration of ~9 days and a large eastward speed of  
378 about 1.5 m/s (Fig. 8e). The UB duration difference of ~2 (3) days is significant at the 90%  
379 (95%) confidence level based on a Monte-Carlo test with 5000 simulations. These UB  
380 differences in longitudinal position, movement and duration lead to a large difference in the

381 cold anomaly in the upstream and downstream sides of central Eurasia between AMO<sup>+</sup> and  
382 AMO<sup>-</sup> (Fig. 8c). Thus, a comparison of Fig. 7 with Fig. 8 reveals that although AMO<sup>+</sup> plays an  
383 important role in the downstream cold anomaly associated with the UBs (Fig. 8b) because of  
384 the long lifetime, eastward movement, slow growth and rapid decay of the composite UB, the  
385 UB-induced sub-seasonal ECA is located more west- and south-ward during IPO<sup>-</sup> than during  
386 AMO<sup>+</sup>, whereas AMO<sup>-</sup> contributes to the upstream cold anomaly through retrograde UBs with  
387 a slow decay.

388 *c. Is the change of the winter ECA from 1965-1976 to 2002-2013 due to interdecadal changes*  
389 *of UB-induced sub-seasonal ECAs modulated by IPO and AMO?*

390 Because 1965-1976 includes both IPO<sup>-</sup> and AMO<sup>-</sup> winters and 2002-2013 corresponds to  
391 both IPO<sup>-</sup> and AMO<sup>+</sup> winters, it is instructive to examine the change of the UB-induced  
392 sub-seasonal ECA from IPO<sup>-</sup> to AMO<sup>+</sup> or from IPO<sup>-</sup> to AMO<sup>-</sup> to understand whether the change  
393 of the winter ECA from 1965-1976 to 2002-2013 is mainly related to the interdecadal changes  
394 of UB-induced sub-seasonal ECAs modulated by IPO<sup>-</sup>, AMO<sup>-</sup> and AMO<sup>+</sup>. We show time-mean  
395 composites of the daily Z500 and SAT anomalies averaged from lag -10 to 10 days of UB  
396 events for IPO<sup>-</sup> during 1965-1976 and AMO<sup>+</sup> during 2002-2013 in Figs. 9a-b. Their difference  
397 fields between 1950-2017 and 1965-1976 for IPO<sup>-</sup>, between 1950-2017 and 2002-2013 for  
398 AMO<sup>+</sup>, between IPO<sup>-</sup> and AMO<sup>+</sup> during 1950-2017, and between IPO<sup>-</sup> during 1965-1976 and  
399 AMO<sup>+</sup> during 2002-2013 are shown in Figs. 9c-f. It is found that the UB-induced cold anomaly  
400 mainly occurs over central Eurasia and its upstream side for IPO<sup>-</sup> during 1965-1976 (Fig. 9a),  
401 but over central Eurasia and its downstream side for AMO<sup>+</sup> during 2002-2013 (Fig.9b).

402 Although Fig. 9c shows that for IPO<sup>-</sup> the strength of the UB-induced cold anomaly is slightly  
403 stronger during 1965-1976 than during 1950-2017, the spatial structure of the cold anomaly  
404 during 1965-1976 is consistent with that during 1950-2017. A similar feature is found for  
405 AMO<sup>+</sup> (Fig. 9d). This result leads us to infer that the spatial structure of the UB-induced cold  
406 anomaly over Eurasia does not strongly depend on the sample size of the UB events, but is  
407 significantly influenced by the phase of IPO or AMO. We also found that the IPO<sup>-</sup> minus  
408 AMO<sup>+</sup> difference during 1950-2017 (Fig.9e) resembles the difference between IPO<sup>-</sup> during  
409 1965-1976 and AMO<sup>+</sup> during 2002-2013 (Fig. 9f). Thus, the decadal variation of UB-induced  
410 cold anomaly from 1965-1976 to 2002-2013 can be, to a large extent, explained by the change  
411 of the UB events associated with the transition from IPO<sup>-</sup> to AMO<sup>+</sup> during 1950-2017.

412 We show the time series of domain-averaged composite daily SAT anomalies over the  
413 upstream (30°-70°E, 30°-50°N) and downstream (90°-130°E, 30°-50° N) regions of the UB  
414 events during the blocking life cycle (from lag -20 to 20 days) for IPO<sup>-</sup>, AMO<sup>-</sup> and AMO<sup>+</sup> in  
415 Figs. 10a-f during 1950-2018, 1965-1976 and 2002-2013. It is found that UBs during AMO<sup>-</sup>  
416 and IPO<sup>-</sup> contribute to strong cold anomalies in the upstream region of central Eurasia (Figs.  
417 10a, c). IPO<sup>-</sup> (Fig. 10a) plays a more important role in the UB-induced cold anomaly in the  
418 upstream side of Eurasia than AMO<sup>-</sup> or AMO<sup>+</sup> (Fig. 10c), even though the upstream cold  
419 anomaly is stronger during 1965-1976 (blue line in Fig.10e) than during 1950-2017 (blue line  
420 in Fig.10a). During 1965-1976, the UB-induced cold anomaly also extends more to the west  
421 and south of Eurasia for IPO<sup>-</sup> than AMO<sup>-</sup> as seen from the IPO<sup>-</sup> minus AMO<sup>-</sup> difference (Fig.  
422 S4) because UB has longer lifetime for IPO<sup>-</sup> (Fig. 7d) than AMO<sup>-</sup> (Fig. 8d). UB events during

423 AMO<sup>+</sup> contribute slightly more to the cold anomaly downstream of Eurasia than during IPO<sup>-</sup>  
424 and AMO<sup>-</sup> (Figs. 10b, d, f). These results suggest that the decadal change of the winter ECA  
425 from 1965-1976 to 2002-2013 (Fig.1d) is not only related to the interdecadal variations of the  
426 UB-induced sub-seasonal ECAs modulated by IPO<sup>-</sup> and AMO<sup>+</sup>, but also related to retrograde  
427 UBs during AMO<sup>-</sup> winters.

428 The above results clearly indicate that IPO<sup>-</sup> has an important impact on the cold anomaly  
429 over the upstream region and southwestern Eurasia through the rapid growth and slow decay of  
430 westward-displaced UB, whereas AMO<sup>+</sup> exerts a large effect on the cold anomaly over the  
431 downstream region through the eastward movement, slow growth and rapid decay of the UBs.  
432 As noted below, the IPO and AMO can influence the UB through different background  
433 conditions. Thus, these different effects of IPO<sup>-</sup> or AMO<sup>-</sup> and AMO<sup>+</sup>, combined with the  
434 interdecadal variations in the UB events, can lead to interdecadal changes in the spatial patterns  
435 of the winter ECA.

436 Because the IPO<sup>-</sup> winters includes AMO<sup>-</sup> and AMO<sup>+</sup> as well as the AMO<sup>+</sup> winters includes  
437 IPO<sup>-</sup> and IPO<sup>+</sup>, it is also useful to examine how the different IPO/AMO combinations modulate  
438 the UB and UB-induced sub-seasonal ECA. Following the above definition of the IPO and  
439 AMO phase combination we show winter UB events during IPO<sup>-</sup>/AMO<sup>-</sup>, IPO<sup>-</sup>/AMO<sup>+</sup>,  
440 IPO<sup>+</sup>/AMO<sup>-</sup> and IPO<sup>+</sup>/AMO<sup>+</sup> winters in Fig.11a. It is found that there are 10 IPO<sup>-</sup>/AMO<sup>-</sup>, 24  
441 IPO<sup>-</sup>/AMO<sup>+</sup>, 22 IPO<sup>+</sup>/AMO<sup>-</sup> and 8 IPO<sup>+</sup>/AMO<sup>+</sup> combination winters during 1950-2017, which  
442 correspond in turn to 25, 43, 42 and 16 UB events or 2.5, 1.79, 1.91 and 2 UB events per winter  
443 (Fig.11a). We show time-mean composite daily Z500 and SAT anomalies averaged from lag -10

444 to 10 days of UB events in Figs. 11b-g for these combinations. We can see that UB events are  
445 most frequent in the IPO<sup>-</sup>/AMO<sup>-</sup> winters and occurred during 1969-1978. In the IPO<sup>-</sup>/AMO<sup>+</sup>  
446 winters UB events occurred during 1950-1959 and 2000-2014 (Fig. 11a). The UB corresponds  
447 to strong sub-seasonal cold anomalies over central Eurasia for the IPO<sup>-</sup>/AMO<sup>-</sup> and IPO<sup>-</sup>/AMO<sup>+</sup>  
448 combinations (Figs.11b-c), although this cold anomaly is stronger and located more southwest  
449 in the IPO<sup>-</sup>/AMO<sup>-</sup> winter (Fig. 11b) than in the IPO<sup>-</sup>/AMO<sup>+</sup> winter (Fig. 11c). In contrast, the  
450 UB-induced cold anomalies are weak over central Eurasia in the IPO<sup>+</sup>/AMO<sup>-</sup> and IPO<sup>+</sup>/AMO<sup>+</sup>  
451 combination winters (Figs. 11e-f). The UB-induced cold anomaly for the IPO<sup>-</sup>/AMO<sup>-</sup>  
452 combination has a spatial pattern similar to that for IPO<sup>-</sup> or AMO<sup>-</sup> in 1965-1976 (Figs. 10a, d).  
453 In the IPO<sup>-</sup>/AMO<sup>+</sup> combination winter, the UB-induced cold anomaly pattern (Fig. 11c) is  
454 analogous to that for the AMO<sup>+</sup> (Fig. 8b). It is further found that the difference of the  
455 UB-induced SAT anomaly field between the IPO<sup>-</sup>/AMO<sup>-</sup> and IPO<sup>-</sup>/AMO<sup>+</sup> combination winters  
456 (Fig. 11d) has a large similarity with the IPO<sup>-</sup> minus AMO<sup>+</sup> difference (Fig. 9e) or the AMO<sup>-</sup>  
457 minus AMO<sup>+</sup> difference (Fig. 8c), even though the AMO<sup>-</sup> minus AMO<sup>+</sup> difference is relatively  
458 weak. To some extent, the change of the UB-induced ECA from the IPO<sup>-</sup>/AMO<sup>-</sup> combinations  
459 during 1965-1976 to the IPO<sup>-</sup>/AMO<sup>+</sup> combinations during 2002-2013 is also similar to the  
460 interdecadal change of UB-induced sub-seasonal ECA from IPO<sup>-</sup> to AMO<sup>+</sup> or from AMO<sup>-</sup> to  
461 AMO<sup>+</sup>. A similar result is found for the IPO/AMO combination based on the 0.5 STD  
462 definition (Fig.S5).

## 463 **5. Atmospheric link between IPO/AMO and Ural blocking and ECA**

464 In this section, we reveal why the phase of IPO or AMO can modulate the UB and why a

465 large SIC decline over BKS is unnecessary for the change of UB during IPO<sup>-</sup>, which occurred  
466 during 1965-1976, but necessary for the UB change during AMO<sup>+</sup>, which occurred during  
467 2002-2013.

468 Figure 12 shows the regression patterns of DJF-mean U500, PV<sub>y</sub> at 500 hPa and SIC  
469 anomalies against the 9-year smoothed DJF-mean IPO and AMO indices shown in Figs. 4a-b.  
470 It is seen that during IPO<sup>-</sup> there are negative U500 anomalies in the North Atlantic mid-high  
471 latitudes (42°-60°N) with a center near 50°N to the north of the Gulf Stream Extension (GSE)  
472 and over Eurasian high latitudes (north of 50°N) (Fig.12a). But during AMO<sup>+</sup> there is a positive  
473 U500 anomaly over the high latitudes (50°-65°N) centered near 60°N to the north of GSE and a  
474 negative anomaly over the Ural Mountains and their east side (Fig. 12b). A reversed westerly  
475 wind pattern is seen for IPO<sup>+</sup> or AMO<sup>-</sup>. The zonal wind patterns during IPO<sup>-</sup> are consistent with  
476 the result of Dong and Dai (2015, their Fig.11). While PV<sub>y</sub> is weak (strong) in the North  
477 Atlantic mid-high latitudes for IPO<sup>-</sup> (AMO<sup>+</sup>), it is weak in Eurasian high latitudes near the Ural  
478 region (Figs. 12c-d). Although the negative U500 or PV<sub>y</sub> anomaly is insignificant over the  
479 North Atlantic for IPO<sup>-</sup> (Fig. 12a) and over the Ural region for AMO<sup>+</sup> (Fig. 12b), their  
480 differences between IPO<sup>-</sup> and AMO<sup>+</sup> are statistically significant ( $p < 0.05$ ) based on a two-sided  
481 Student t-test (not shown). Thus, the North Atlantic zonal wind and PV<sub>y</sub> patterns show opposite  
482 changes between IPO<sup>-</sup> and AMO<sup>+</sup>, although they are weak in the Ural region. In summary,  
483 weak zonal winds and small PV<sub>y</sub> are seen in the region from the south side of Greenland to the  
484 Ural region and its east side for IPO<sup>-</sup>. But for AMO<sup>+</sup> zonal winds and PV<sub>y</sub> are strong in the  
485 south side of Greenland and weak in the Ural region.

486 According to the theoretical result of Zhang and Luo (2020), the UB shows rapid growth  
487 and slow decay when upstream background westerly winds and  $PV_y$  are weak as seen during  
488  $IPO^-$ . In contrast, the UB shows an enhanced eastward movement, slow growth and rapid decay  
489 when upstream background westerly winds and  $PV_y$  are relatively strong as seen during  $AMO^+$ .  
490 Thus, these results explain why the UB shows an opposite change in movement and evolution  
491 between  $IPO^-$  and  $AMO^+$  as seen in Figs. 7d and 8e. We also see that weak high-latitude  
492 westerly winds and small  $PV_y$  over Eurasia can occur without strong BKS warming or SIC  
493 decline for  $IPO^-$  (Luo et al. 2019a) because  $IPO^-$  corresponds to an interdecadal cold anomaly  
494 in Eurasian high latitudes (the north of  $60^\circ N$ ) (Figs. 5b) as seen during 1965-1976 (Fig. 1e).  
495 Thus, the BKS SIC anomaly may be positive for  $IPO^-$  (Fig. 12e), indicating that a low BKS SIC  
496 is not needed for the maintenance of UB for  $IPO^-$ , whereas  $AMO^-$  has a similar effect. But a  
497 large BKS sea-ice loss is needed for increased persistence of UB for  $AMO^+$  (Fig. 12f) because  
498 the warm anomaly background is dominant over Eurasian mid-high latitudes for  $AMO^+$  (Fig. 5d)  
499 as occurred during 2002-2013 (Fig. 1f).

500 The above results explain why a strong winter ECA can occur during 1965-1976 even when  
501  $IPO^-$  or  $AMO^-$  dominates and a large BKS SIC decline is absent (Fig. 12e). In contrast, the BKS  
502 warming and thus SIC decline must be strong for  $AMO^+$  so that the winter ECA can occur  
503 during 2002-2013. Our finding here does not contradict the results of Mori et al. (2014), who  
504 showed a robust Eurasian cooling in the ensemble-mean response to recent Arctic sea-ice loss  
505 (but not in individual realizations), because our result can not only explain why the BKS SIC  
506 decline must be strong for the ECA during 2002-2013, but also explain why the BKS SIC

507 anomaly can be positive for the ECA during 1965-1976. Furthermore, greenhouse gas-induced  
508 warming and sea-ice loss are unlikely to cause cooling over Eurasia (Dai and Song 2020); thus,  
509 the ECA more likely results from internal decadal variations of UB associated with internal  
510 modes such as the IPO, AMO and Arctic decadal variations.

511 The above results reveal that AMO<sup>+</sup> favors eastward-moving, slowly growing and rapidly  
512 decaying UBs over Eurasia through the intensifying (weakening) of high-latitude westerly  
513 winds and PV<sub>y</sub> over the North Atlantic (Eurasia), whereas IPO<sup>-</sup> promotes the slow westward-  
514 moving, rapidly growing and slowly decaying UBs through the weakening of high-latitude  
515 westerly winds and PV<sub>y</sub> from the North Atlantic to Eurasia. But UBs are relatively short-lived  
516 and retrograde during AMO<sup>-</sup> and IPO<sup>+</sup> because the zonal winds and PV<sub>y</sub> conditions are opposite  
517 to those during AMO<sup>+</sup> and IPO<sup>-</sup>.

## 518 **6. Summary and Conclusions**

519 In this paper, we first examined the dependence of winter Ural blocking (UB) and its  
520 impact on Eurasian surface air temperature (SAT) on the phase of IPO and AMO as defined by  
521 9-year smoothed IPO and AMO indices, and then combined the recent IPO and AMO phases to  
522 physically explain the interdecadal difference in the winter Eurasian cold anomaly (ECA)  
523 between 1965-1976 and 2002-2013. A strong winter ECA is found to occur more in the  
524 upstream and southwestern side of central Eurasia during 1965-1976 than during 2002-2013.  
525 This interdecadal change is found to be mainly related to IPO<sup>-</sup> and AMO<sup>+</sup> through their  
526 modulation of the Ural blocking (UB) in its movement, persistence and evolution (rather than  
527 in its event numbers), whereas AMO<sup>-</sup> contributes to the 1965-1976 ECA through retrograde

528 slowly decaying UBs. In contrast, without the UB the impact of IPO<sup>-</sup> and AMO<sup>-</sup> on the cold  
529 SAT anomaly is mainly confined to the north of 60°N over Eurasia. We propose a new pathway  
530 of the IPO/AMO–ECA connection, which works by means of the UB change due to the  
531 changed background condition associated with the phase of the IPO or AMO: different  
532 IPO/AMO phases lead to different background conditions in zonal winds and PV<sub>y</sub> over the  
533 North Atlantic and Eurasia, which affect the characteristics of UB, which in turn affect SAT  
534 over Eurasia through cold advection.

535         The 1965-1976 period was dominated by a negative phase IPO (IPO<sup>-</sup>) in combination with  
536 a negative phase AMO (AMO<sup>-</sup>), while a positive phase AMO (AMO<sup>+</sup>) in combination with  
537 IPO<sup>-</sup> are frequent during 2002-2013. Although the event frequency of winter UB events does  
538 not strongly depend on the phase of IPO or AMO during 1950-2017, we found that the UB is  
539 long-lived and shows rapid growth, slow decay and retrogression during the decaying phase  
540 (eastward movement, slow growth and rapid decay) during IPO<sup>-</sup> (AMO<sup>+</sup>), but is relatively  
541 short-lived and retrograde during both IPO<sup>+</sup> and AMO<sup>-</sup>. During IPO<sup>-</sup> the UB leads to a strong  
542 cold anomaly with a southwestward extension of central Eurasia through advection of cold  
543 Arctic air into these regions. During AMO<sup>+</sup> the UB induces strong cold anomalies over central  
544 Eurasia and its downstream side through advection of cold Arctic air. It is found that the change  
545 of the winter ECA from 1965-1976 to 2002-2013 is mainly related to the different influences of  
546 the IPO<sup>-</sup>, AMO<sup>-</sup> and AMO<sup>+</sup> on the longitudinal position, persistence, movement and evolution  
547 of UB. The difference of the UB-induced sub-seasonal cold anomaly between the IPO<sup>-</sup>/AMO<sup>-</sup>  
548 and IPO<sup>-</sup>/AMO<sup>+</sup> combination winters more resembles the IPO<sup>-</sup> minus AMO<sup>+</sup> difference than

549 the AMO<sup>-</sup> minus AMO<sup>+</sup> difference.

550 It is further revealed that during IPO<sup>-</sup> without UB the background zonal winds and  
551 meridional PV gradient ( $PV_y$ ) over Eurasian high latitudes are weakened due to reduced  
552 meridional temperature gradients and intensified PV anomalies related to strong background  
553 cold anomaly in the high-latitude Eurasia (Fig. 5b) without strong warming or SIC decline over  
554 Barents-Kara Seas (BKS). Such zonal wind and  $PV_y$  changes over Eurasian high latitudes favor  
555 long-lived UBs, which are also seen during AMO<sup>+</sup> and related to a strong warming or SIC  
556 decline in BKS because the background warm anomaly prevails over Eurasian mid-high  
557 latitudes. During IPO<sup>-</sup> (AMO<sup>+</sup>) weakened (intensified) westerly winds are also seen over the  
558 North Atlantic high latitudes because of the presence of weak positive Z500 anomalies over the  
559 North Atlantic north (south) of 60°N (Dong and Dai 2015), which lead to the rapid growth,  
560 slow decay and retrogression of UB during its decaying phase (slow growth, rapid decay and  
561 eastward movement of UB) during IPO<sup>-</sup> (AMO<sup>+</sup>). The reversed zonal wind patterns are seen for  
562 IPO<sup>+</sup> (AMO<sup>-</sup>).

563 In summary, our main results are that the large difference in UB's position, movement and  
564 evolution between IPO<sup>-</sup>, AMO<sup>-</sup> and AMO<sup>+</sup> is important for the interdecadal variation of the  
565 winter ECA from 1965-1976 to 2002-2013. A large BKS warming (or SIC decline) is necessary  
566 for the generation of the winter ECA for AMO<sup>+</sup>, but is not necessary for IPO<sup>-</sup>. Rudeva and  
567 Simmonds (2021) have also pointed to the role of the high-latitude background wind field in  
568 permitting or denying the establishment of quasi-stationary teleconnection patterns.  
569 Specifically, IPO<sup>-</sup> influences the ECA via the following pathway: IPO<sup>-</sup>→weak westerly winds

570 and small  $PV_y$  over Eurasian high latitudes and North Atlantic mid-high latitudes→long-lived  
571 and westward-shifted UB with rapid growth and slow decay→upstream ECA. In contrast,  
572  $AMO^+$  influences the ECA via the following pathway:  $AMO^+$ →weak westerly winds and small  
573  $PV_y$  over Eurasian high latitudes as well as strong zonal winds and large  $PV_y$  over North  
574 Atlantic high latitudes (different from those over the North Atlantic for  $IPO^-$ )→long-lived UB  
575 with eastward movement, slow growth and rapid decay→downstream ECA. Thus, the role of  
576  $AMO^+$  is to cause long-lived UB with eastward movement, slow growth and rapid decay and  
577 downstream ECA through enhancing upstream zonal winds and  $PV_y$ , whereas the role of  $IPO^-$   
578 is to cause long-lived UB occurring in the upstream side of the Ural region with rapid growth  
579 and slow decay and upstream ECA through reduced upstream zonal winds and  $PV_y$ . These  
580 different roles of  $IPO^-$ ,  $AMO^-$  and  $AMO^+$  in the longitudinal position, movement and evolution  
581 of the UB and ECA and in the change of the winter ECA from 1965-1976 to 2002-2013 are not  
582 revealed in previous studies (e.g., Luo et al. 2017b; Sung et al. 2018; B. Luo et al. 2019).

583 Although the NECP reanalysis data from 1950-2017 used in this paper is relatively short for  
584 sampling the IPO or AMO, the obtained results are reliable because the used data include one  
585 cycle of the AMO or at least one cycle for the IPO. However, further study is needed using long  
586 reanalysis and model data.

587

## 588 **Acknowledgements**

589 This manuscript was finished before 2020. This research was supported by the Chinese  
590 Academy of Sciences Strategic Priority Research Program (Grant XDA19070403), National  
591 key research and development program of China (2016YFA0601802) and the National Natural

592 Science Foundation of China (Grant numbers: 41790473 and 41430533). A. Dai acknowledges  
593 the funding support from the U.S. National Science Foundation (Grant Nos. AGS-2015780 and  
594 OISE-1743738). The NCEP- NCAR reanalysis data is from [https://www.esrl.noaa.gov/  
595 psd/data/gridded/data.ncep.reanalysis](https://www.esrl.noaa.gov/psd/data/gridded/data.ncep.reanalysis), the SST data is taken from [http://www.metoffice.gov.uk/  
596 hadobs/hadisst/data/](http://www.metoffice.gov.uk/hadobs/hadisst/data/), the IPO and AMO indices are available from [https://climexp.knmi.nl/  
597 selectindex.cgi?id=someone@\\_somewhere](https://climexp.knmi.nl/selectindex.cgi?id=someone@_somewhere) and the daily NAO index is taken from [https:  
598 //www.cpc.noaa.gov/products/precip/CWlink/pna/nao.shtml](https://www.cpc.noaa.gov/products/precip/CWlink/pna/nao.shtml).

599

600 **References:**

601

602 Booth, B. B. B., Dunstone, N. J., Halloran, P. R., Andrews, T., & Bellouin, N., 2012: Aerosols  
603 implicated as a prime driver of twentieth-century North Atlantic climate variability.

604 *Nature*, **484**, 228–232. <https://doi.org/10.1038/nature10946>

605 Chen, X., and K.-K. Tung, 2014: Varying planetary heat sink led to global-warming slowdown  
606 and acceleration. *Science*, **345**, 897–903, <https://doi.org/10.1126/science.1254937>.

607 Chylek, P., C. K. Folland, G. Lesins, M. K. Dubey, and M. Wang, 2009: Arctic air temperature  
608 change amplification and the Atlantic Multidecadal Oscillation. *Geophys.Res. Lett.*, **36**,

609 L14801,doi:[10.1029/2009GL038777](https://doi.org/10.1029/2009GL038777).

610 Cohen, J. L., J. C. Furtado, M. A. Barlow, V. A. Alexeev, and J. E. Cherry, 2012: Arctic  
611 warming, increasing fall snow cover and widespread boreal winter cooling, *Environ. Res.*

612 *Lett.*, **7**, 014007, doi:[10.1088/1748-9326/7/1/014007](https://doi.org/10.1088/1748-9326/7/1/014007).

613 Cohen, J., and Coauthors, 2014: Recent Arctic amplification and extreme mid-latitude weather.

614 *Nat. Geosci.*, **7**, 627–637, <https://doi.org/10.1038/ngeo2234>.

615 Dai, A., 2013: The influence of the inter-decadal Pacific oscillation on US precipitation during  
616 1923–2010. *Clim Dyn* 41:633–646. <https://doi.org/10.1007/s00382-012-1446-5>

617 Dai, A., J. C. Fyfe, S.-P. Xie, and X. Dai, 2015: Decadal modulation of global surface  
618 temperature by internal climate variability. *Nat. Climate Change*, **5**, 555–559,  
619 <https://doi.org/10.1038/nclimate2605>.

620 Dai, A., and M. Song, 2020: Little influence of Arctic amplification on midlatitude climate.  
621 *Nature Climate Change*, **10**, 231–237. <https://doi.org/10.1038/s41558-020-0694-3>.

622 Delworth, T. L., and M. E. Mann, 2000: Observed and simulated multidecadal variability in the  
623 Northern Hemisphere. *Climate Dyn.*, 16,661–676,<https://doi.org/10.1007/s003820000075>.

624 Deser, D., and M. Blackmon, 1995: On the relationship between tropical and North Pacific sea  
625 surface temperature variations. *J. Climate*, **8**,1677–1680.

626 Deser, C., Guo, R., and Lehner, F. 2017: The relative contributions of tropical Pacific sea  
627 surface temperatures and atmospheric internal variability to the recent global warming  
628 hiatus, *Geophys. Res. Lett.*, 44, 7945– 7954, doi:[10.1002/2017GL074273](https://doi.org/10.1002/2017GL074273).

629 Diao Y., J. Li and D. Luo, 2006: A new blocking index and its application: Blocking action in  
630 the Northern Hemisphere, *J. Climate*, **19**, 4819-4839.

631 Dong, B. and A. Dai, 2015: The influence of the Interdecadal Pacific Oscillation on  
632 Temperature and Precipitation over the Globe, *Climate Dyn.*, **45**, 2667. [https://doi.org](https://doi.org/10.1007/s00382-015-2500-x)  
633 [/10.1007/s00382-015-2500-x](https://doi.org/10.1007/s00382-015-2500-x)

634 Dong, B., A. Dai, M. Vuille, and O. Elison Timm, 2018: Asymmetric modulation of ENSO  
635 teleconnections by the Interdecadal Pacific Oscillation. *J. Climate*, **31**:7337-7361.

636 <https://doi.org/10.1175/JCLI-D-17-0663.1>.

637 Hua, W., A. Dai, and M. Qin, 2018: Contributions of internal variability and external forcing to  
638 the recent Pacific decadal variations. *Geophys. Res. Lett.*, **45**, 7084–7092.  
639 <https://doi.org/10.1029/2018GL079033>.

640 Hua W., Dai A., Zhou L., Qin M., and H. Chen, 2019. An externally-forced decadal rainfall  
641 seesaw pattern over the Sahel and southeast Amazon., *Geophys. Res. Lett.*, **46**, 923–932.  
642 <https://doi.org/10.1029/2018GL081406>

643 Huang D., A. Dai, Yang B., et al., 2019: Contributions of different combinations of the IPO and  
644 AMO to recent changes in winter East Asian jets. *J. Climate*, **32**, 1607-1625.

645 Huang, J. P., Y. K. Xie, X. D. Guan, D. D. Li, and F. Ji, 2017: The dynamics of the warming  
646 hiatus over the northern hemisphere, *Climate Dyn.*, **48**, 429–446, doi:10.1007/s00382-  
647 016-3085-8.

648 Kalnay, E., and Coauthors, 1996: The NCEP/NCAR 40-Year Reanalysis project. *Bull. Amer.*  
649 *Meteor. Soc.*, **77**, 437–471, [https://doi.org/10.1175/1520-0477\(1996\)077,0437: TNYRP.](https://doi.org/10.1175/1520-0477(1996)077,0437: TNYRP.2.0.CO;2)  
650 [2.0.CO;2](https://doi.org/10.1175/1520-0477(1996)077,0437: TNYRP.2.0.CO;2).

651 Kaplan, A., M. A. Cane, Y. Kushnir, A. C. Clement, M. B. Blumenthal, and B. Rajagopalan,  
652 1998: Analyses of global sea surface temperature 1856–1991. *J. Geophys. Res.*, **103**, 18  
653 567–18 589, <https://doi.org/10.1029/97JC01736>.

654 Karl, T. R., and Coauthors, 2015: Possible artifacts of data biases in the recent global surface  
655 warming hiatus. *Science*, **348**, 1469–1472, <https://doi.org/10.1126/science.aaa5632>.

656 Kaufmann, R. K., Kauppi, H., Mann, M. L., and J. H. Stock, 2011: Reconciling anthropogenic

657 climate change with observed temperature 1998-2008. *Proc. Natl Acad. Sci. USA*, **108**,  
658 11790-11793.

659 Kim, H.-J., S.-W. Son, W. Moon, J.-S. Kug and J. Hwang, 2021: Subseasonal relationship  
660 between Arctic and Eurasian surface air temperature. *Scientific Reports*, 11, 4081, doi:  
661 10.1038/s41598-021-83486-5

662 Kosaka, Y., and S.-P. Xie, 2013: Recent global-warming hiatus tied to equatorial Pacific  
663 surface cooling. *Nature*, **501**, 403–407, <https://doi.org/10.1038/nature12534>.

664 Li, C., B. Stevens, and J. Marotzke, 2015: Eurasian winter cooling in the warming hiatus of  
665 1998–2012, *Geophys. Res. Lett.*, *42*, 8131–8139, doi:10.1002/2015GL065327.

666 Li, M., D. Luo, I. Simmonds, A. Dai, L. Zhong and Y. Yao, 2021: Anchoring of atmospheric  
667 teleconnection patterns by Arctic Sea ice loss and its link to winter cold anomalies in East  
668 Asia. *International Journal of Climatology*, **41**, 547–558, doi: 10.1002/joc.6637.

669 Luo, B., D. Luo, L. Wu, L. Zhong, and I. Simmonds, 2017: Atmospheric circulation patterns  
670 which promote winter Arctic sea ice decline. *Environ. Res. Lett.*, *12*, 054017,  
671 <https://doi.org/10.1088/1748-9326/aa69d0>.

672 Luo, B., L., Wu, D. Luo, A. Dai and I. Simmonds, 2019: The winter midlatitude-Arctic  
673 interaction: effects of North Atlantic SST and high-latitude blocking on Arctic sea ice and  
674 Eurasian cooling. *Climate Dynamics* **52**:5-6, 2981-3004.

675 Luo, D., A. R. Lupo and H. Wan, 2007: Dynamics of Eddy-Driven Low-Frequency Dipole  
676 Modes. Part I: A Simple Model of North Atlantic Oscillations. *J. Atmos. Sci.*, **64**, 3-28.

677 Luo, D., Y. Yao and A. Dai, 2015: Decadal relation between European blocking and North  
678 Atlantic Oscillation during 1978-2011. Part I: Atlantic conditions. *J. Atmos. Sci.*,  
679 72,1152-1173.

680 Luo, D., Y. Xiao, Y. Yao, A. Dai, I. Simmonds, and C. L. E. Franzke, 2016a: Impact of Ural  
681 blocking on winter warm Arctic–cold Eurasian anomalies. Part I: Blocking induced  
682 amplification. *J. Climate*, 29, 3925–3947, <https://doi.org/10.1175/JCLI-D-15-0611.1>.

683 Luo, D., Y. Xiao, Y. Diao, A. Dai, C. L. E. Franzke and I. Simmonds, 2016b: Impact of Ural  
684 Blocking on winter Warm Arctic–Cold Eurasian anomalies. Part II: The link to the North  
685 Atlantic Oscillation. *J. Climate*, **29**, 3949-3971, doi: 10.1175/JCLI-D-15-0612.1.

686 Luo, D., Y. Yao, A. Dai, I. Simmonds and L. Zhong, 2017a: Increased quasi-stationarity and  
687 persistence of winter Ural Blocking and Eurasian extreme cold events in response to  
688 Arctic warming. Part II: A theoretical explanation. *J. Climate*, **30**, 3569–3587, doi:  
689 10.1175/JCLI-D-16-0262.1.

690 Luo, D., Y. Chen, A. Dai, M. Mu, R. Zhang and I. Simmonds, 2017b: Winter Eurasian cooling  
691 linked with the Atlantic Multidecadal Oscillation, *Environ. Res. Lett.*, **12**, 125002.

692 Luo, D., X. Chen, A. Dai and I. Simmonds 2018: Changes in atmospheric blocking circulations  
693 linked with winter Arctic warming: A new perspective. *J. Climate*, **31**, 7661-7677

694 Luo, D., X. Chen and S. Feldstein, 2018b: Linear and nonlinear dynamics of North Atlantic  
695 Oscillations: A new thinking of symmetry breaking, *J. Atmos. Sci.*, **75**, 1955-1977, DOI:  
696 10.1175/JAS- D-17-0274.1

697 Luo, D., X. Chen, J. Overland, I. Simmonds, Wu, Y. and P. Zhang, 2019a: Weakened potential  
698 vorticity barrier linked to recent winter Arctic sea ice loss and midlatitude cold extremes. *J.*  
699 *Climate*, **32**, 4235-4261.

700 Luo, D., W. Zhang, L. Zhong and A. Dai, 2019b: A nonlinear theory of atmospheric blocking: A  
701 potential vorticity gradient view. *J. Atmos. Sci.*, **76**, 2399-2427.

702 Marotzke, J., and P. M. Forster (2015), Forcing, feedback and internal variability in global  
703 temperature trends, *Nature*, **517**, 565–570, [doi:10.1038/nature14117](https://doi.org/10.1038/nature14117).

704 Masato, G., B. J. Hoskins, and T. J. Woollings, 2013a: Wave-breaking characteristics of  
705 Northern Hemisphere winter blocking: A two-dimensional approach. *J. Climate*, **26**,  
706 4535-4549.

707 Masato, G., B. J. Hoskins, and T. J. Woollings, 2013b: Winter and Summer Northern  
708 Hemisphere Blocking in CMIP5 Models. *J. Climate*, **26**, 7044-7059.

709 Meehl, G. A., A. Hu, J. M. Arblaster, J. Fasullo, and K. E. Trenberth, 2013: Externally forced  
710 and internally generated decadal climate variability associated with the interdecadal  
711 Pacific oscillation. *J. Climate*, **26**, 7298–7310, [https://doi.org/10.1175/](https://doi.org/10.1175/JCLI-D-12-00548.1)  
712 [JCLI-D-12-00548.1](https://doi.org/10.1175/JCLI-D-12-00548.1).

713 Meehl, G. A., B. D. Santer, and S.-P. Xie, 2016: Contribution of the interdecadal Pacific  
714 oscillation to twentieth-century global surface temperature trends. *Nat. Climate Change*, **6**,  
715 1005–1008, <https://doi.org/10.1038/nclimate3107>.

716 Meehl, G. A., A. Hu, F. Castruccio and others, 2021: Atlantic and Pacific tropics connected by  
717 mutually interactive decadal-timescale processes. *Nature Geoscience*, **14**, 36–42.

718 Mori, M., M. Watanabe, H. Shiogama, J. Inoue, and M. Kimoto, 2014: Robust Arctic sea-ice  
719 influence on the frequent Eurasian cold winters in past decades. *Nat. Geosci.*, 7, 869–873,  
720 <https://doi.org/10.1038/ngeo2277>.

721 van Oldenborgh, G. J., te Raa, L. A., Dijkstra, H. A., and S. Y. Philip, 2009: Frequency- or  
722 amplitude-dependent effects of the Atlantic meridional overturning on the tropical Pacific  
723 Ocean, *Ocean Sci.*, 5, 293–301, <https://doi.org/10.5194/os-5-293-2009>.

724 Power S, Casey T, Folland C, Colman A., and V. Mehta, 1999: Interdecadal modulation of the  
725 impact of ENSO on Australia. *Climate Dyn.*, 15, 319–324. doi:[10.1007/s003820050284](https://doi.org/10.1007/s003820050284)

726 Rayner, N. A., D. E. Parker, E. B. Horton, C. K. Folland, L. V. Alexander, D. P. Rowell, E. C.  
727 Kent, and A. Kaplan, 2003: Global analyses of sea surface temperature, sea ice, and night  
728 marine air temperature since the late nineteenth century. *J. Geophys. Res.*, 108, 4407,  
729 <https://doi.org/10.1029/2002JD002670>.

730 Rudeva, I., and I. Simmonds, 2021: Midlatitude winter extreme temperature events and  
731 connections with anomalies in the Arctic and tropics. *J. Climate*, 34, 3733–3749, doi:  
732 [10.1175/JCLI-D-20-0371.1](https://doi.org/10.1175/JCLI-D-20-0371.1).

733 Sung, M.-K., S.-H. Kim, B.-M. Kim and Y.-S. Choi, 2018: Interdecadal variability of the  
734 Warm Arctic and Cold Eurasia Pattern and its North Atlantic origin. *J. Climate*, 31,  
735 5793–5810, doi: [10.1175/JCLI-D-17-0562.1](https://doi.org/10.1175/JCLI-D-17-0562.1).

736 Steinman B. A., M. E. Mann and S. K. Miller, 2015: Atlantic and Pacific multidecadal oscillations  
737 and Northern Hemisphere temperatures. *Science*, 347, 988–991. doi:[10.1126/science.](https://doi.org/10.1126/science.1257856)  
738 [1257856](https://doi.org/10.1126/science.1257856)

739 Tibaldi, S., and F. Molteni, 1990: On the operational predictability of blocking. *Tellus*, 42A,  
740 343–365, doi:[10.1034/j.1600-0870.1990.t01-2-00003.x](https://doi.org/10.1034/j.1600-0870.1990.t01-2-00003.x).

741 Trenberth, K. E., and D. J. Shea, 2006: Atlantic hurricanes and natural variability in 2005.  
742 *Geophys. Res. Lett.*, 33, L12704, <https://doi.org/10.1029/2006GL026894>.

743 Trenberth K. E, and J. T, Fasullo, 2013: An apparent hiatus in global warming? *Earth's Future*  
744 1, 19–32. <https://doi.org/10.1002/2013EF000165>.

745 Trenberth, K. E., 2015: Has there been a hiatus. *Science*, **349**, 691–692. [https://doi.org/](https://doi.org/10.1126/science.aac9225)  
746 [10.1126/science.aac9225](https://doi.org/10.1126/science.aac9225).

747 Tyrllis, E, Bader, J, Manzini, E, Ukita, J, Nakamura, H, Matei, D., 2020: On the role of Ural  
748 Blocking in driving the Warm Arctic-Cold Central Eurasia pattern. *Quart. J. R. Meteorol.*  
749 *Soc.*, **146**, 2138- 2153.

750 Tyrllis E, Bader J, Manzini E and D. Matei, 2021: Reconciling different methods of  
751 high-latitude blocking detection. *Quart. J. Roy. Meteor. Soc.* **147**: 1070-1096 doi:  
752 [10.1002/qj.3960](https://doi.org/10.1002/qj.3960).

753 Wyatt, M.G., Kravtsov, S. and A. A. Tsonis, 2012: Atlantic Multidecadal Oscillation and  
754 Northern Hemisphere's climate variability. *Climate Dyn.*, 38: 929-949.

755 Wilks, D. S., 2011, Statistical methods in the atmospheric sciences, 3<sup>rd</sup> Edition, Academic  
756 Press, Oxford.

757 Woollings, T. J., B. J. Hoskins, P. Blackburn, and P. Berrisford, 2008: A new Rossby  
758 wave-breaking interpretation of the North Atlantic Oscillation. *J. Atmos. Sci.*, **65**,  
759 609-626, . doi:[10.1175/2007JAS2347.1](https://doi.org/10.1175/2007JAS2347.1).

760 Yao, Y., D. Luo, A. Dai, and I. Simmonds, 2017: Increased quasi stationarity and persistence  
761 of winter Ural blocking and Eurasian extreme cold events in response to Arctic warming.  
762 Part I: Insights from observational analyses. *J. Climate*, 30, 3549–3568,

763 Wei M, F. Qiao and J. Deng, 2015: A quantitative definition of global warming hiatus and  
764 50-Year prediction of global-mean surface temperature. *J Atmos Sci.*, 72:3281–3289.

765 Zhang, R., and T. L. Delworth, 2007: Impact of the Atlantic multidecadal oscillation on North  
766 Pacific climate variability. *Geophys. Res. Lett.*, **34**, L23708, <https://doi.org/10.1029/2007>  
767 [GL031601](https://doi.org/10.1029/2007GL031601)

768 Zhang, W., and D. Luo, 2020: A Nonlinear theory of atmospheric blocking: An application to  
769 Greenland blocking changes linked to winter Arctic sea ice loss. *J. Atmos. Sci.*, **77**,  
770 723-751.

771  
772  
773  
774  
775  
776  
777  
778  
779  
780  
781  
782  
783  
784  
785  
786  
787  
788  
789  
790  
791

792  
 793  
 794  
 795  
 796  
 797  
 798  
 799  
 800  
 801  
 802  
 803  
 804  
 805  
 806  
 807  
 808  
 809  
 810  
 811  
 812  
 813  
 814  
 815  
 816  
 817  
 818  
 819  
 820  
 821  
 822  
 823  
 824  
 825  
 826  
 827  
 828  
 829

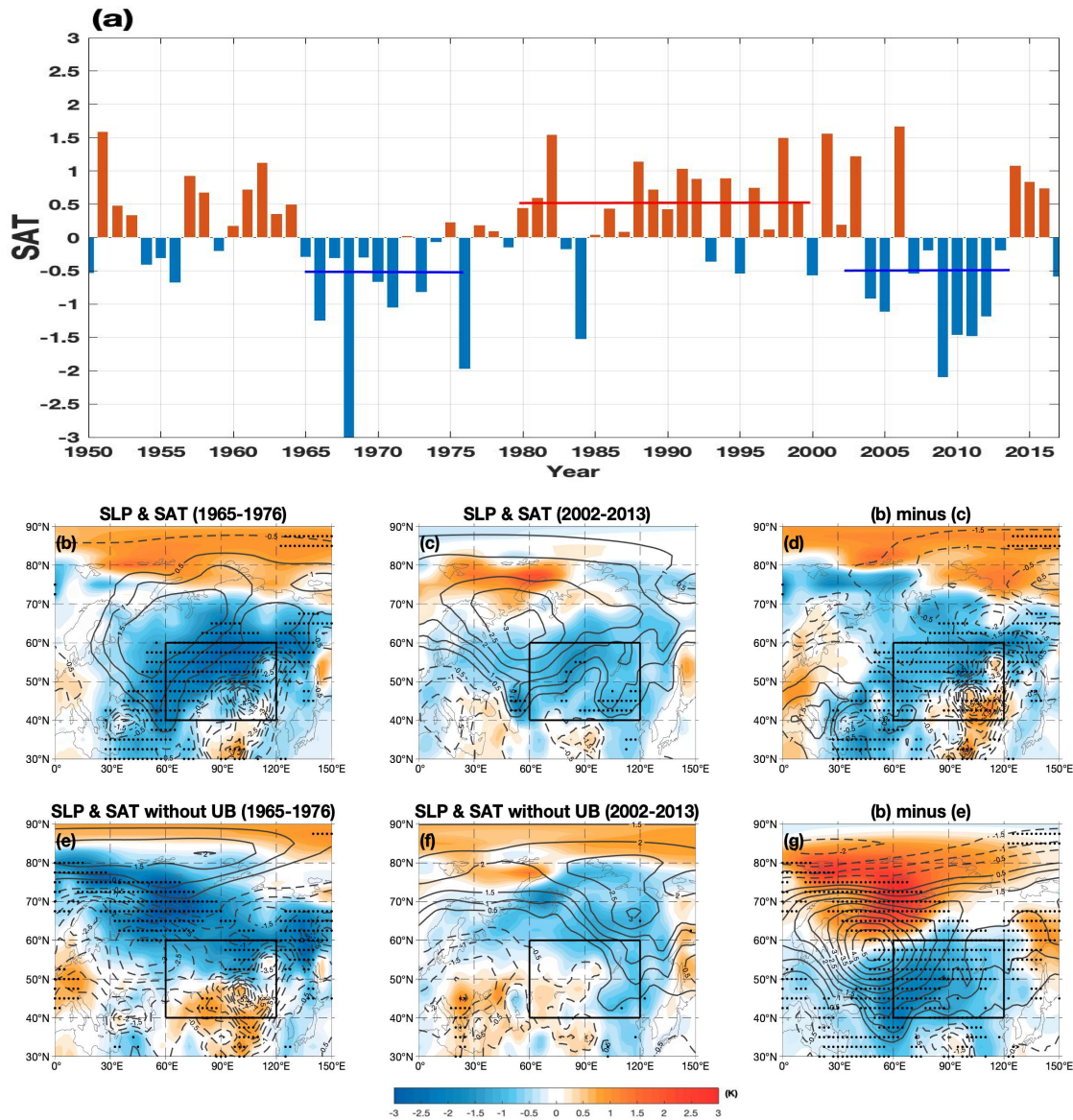
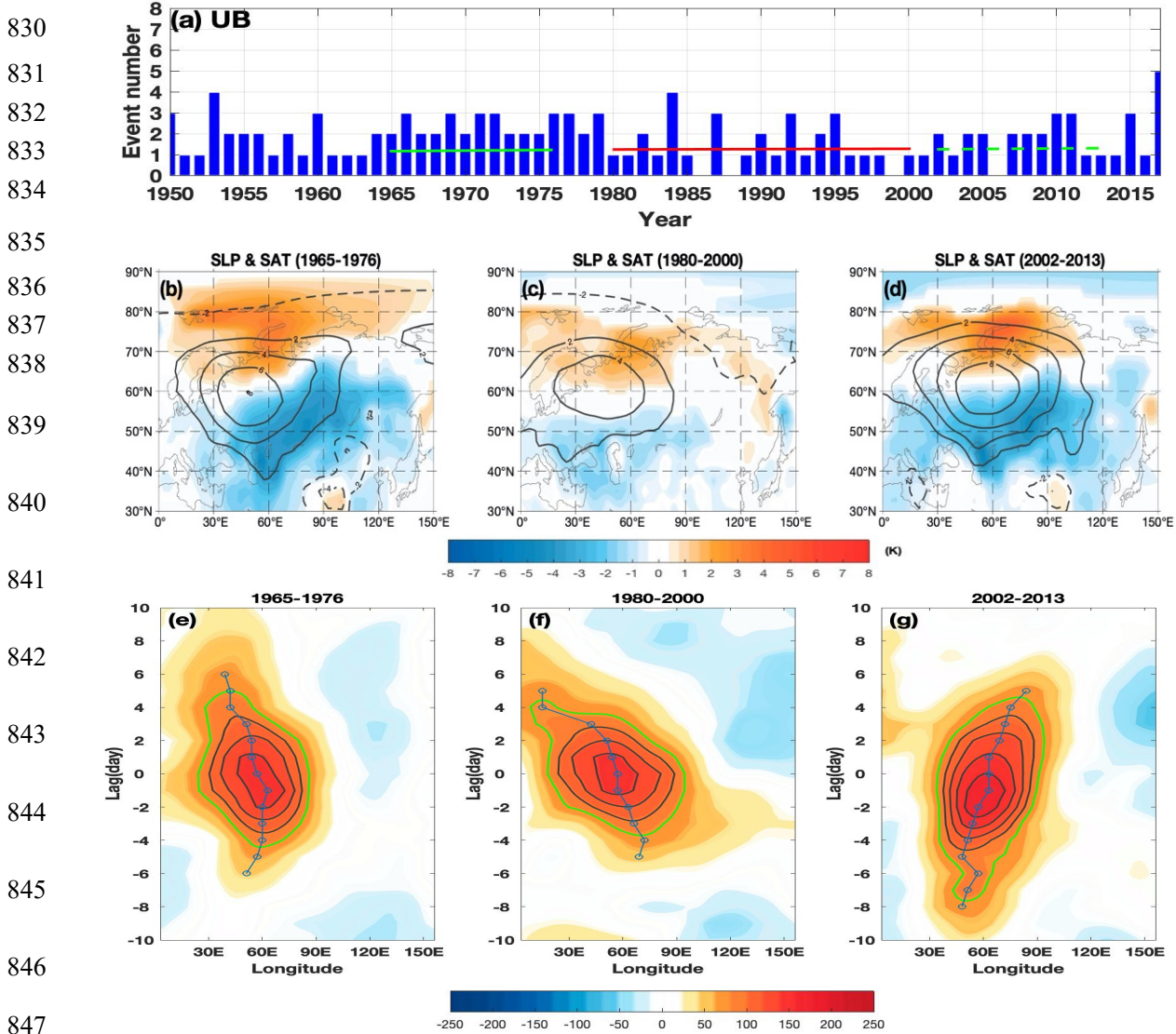


**Figure 1.** (a) Time series of DJF-mean surface air temperature (SAT) anomalies averaged over central Eurasia (60°-120°E, 40°-60°N), with the red line denoting the 1980-2000 period, and the blue line marking the 1965-1976 and 2002-2013 periods. (b, c, d, e, f, g) DJF-mean sea surface pressure (SLP) (contours; contour interval (CI)=0.5 hPa) and SAT (color shading in K) anomalies averaged during (b, e) 1965-1976 and (c, f) 2002-2013 for UB events (b, c) included and (e, f) excluded (blocking days from lag -10 to 10 days are excluded, lag 0 denotes the day of the UB peak) as well as (d) b minus c and (g) b minus e differences. The dot represents the areas of the SAT anomaly being significant at the 95% level based on a two-sided Student t-test. Black box represents central Eurasia.



848 **Figure 2.** (a) Time series of the number of winter Ural blocking (UB) events (a total of 126  
849 cases) during 1950-2017 with three sub-periods: 1965-1976 (29 cases, blue line), 1980-2000  
850 (30 cases; red line) and 2002-2013 (21 cases; dashed green line). (b, c, d) Time-mean  
851 composite daily SLP (contours, CI=2 hPa) and SAT (color shading, in K) anomalies averaged  
852 from lag -10 to 10 days (lag 0 denotes the peak day of blocking) for (b) 29 UB events during  
853 1965-1976, (c) 30 UB events during 1980-2000 and (d) 21 UB events during 2002-2013. (e, f,  
854 g) Time-longitude evolution of the composite daily Z500 anomalies (unit: gpm and CI=20 gpm)  
855 averaged over 50°-70°N of the UB events during (e) 1965-1976, (f) 1980-2000 and (g)  
856 2002-2013. In (e-g), the 80 gpm contour is marked by the green line and the thick blue line  
857 denotes the zonal location of the maximum daily Z500 anomaly whose temporal variation  
858 represents the movement speed. The color shading represents the region above the 95%  
859 confidence level based on a two-sided Student *t*-test.

860  
861  
862  
863  
864  
865  
866  
867  
868  
869  
870  
871  
872  
873  
874  
875  
876  
877  
878  
879  
880  
881  
882  
883  
884  
885  
886  
887  
888  
889  
890  
891  
892  
893  
894  
895  
896  
897  
898  
899  
900  
901  
902

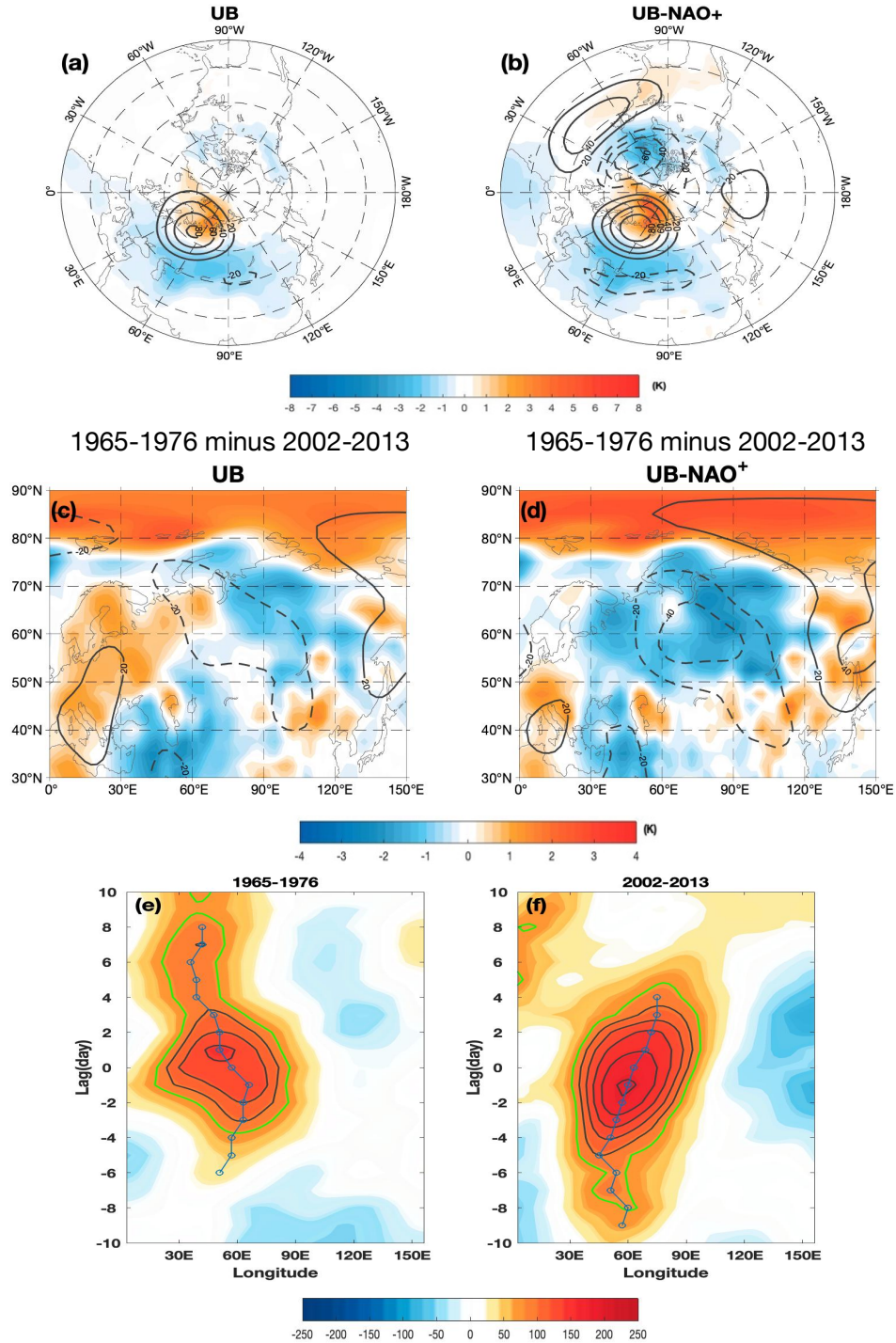


**Figure 3.** Time-mean composite daily 500-hPa geopotential height (Z500) (contours, CI=20 gpm) and SAT (color shading, unit: K) anomalies averaged from lag -10 to 10 days (lag 0 denotes the peak day of blocking) for (a) UB and (b) UB-NAO<sup>+</sup> events during 1950-2017. (c, d) 1965-1976 minus 2002-2013 differences of time-mean Z500 and SAT anomalies for (c) UB and (d) UB-NAO<sup>+</sup> events, where the color shading represents the region above the 95% confidence level based on a two-sided Student t-test. (e, f) Time-longitude evolution of composite daily Z500 anomalies (unit: gpm and CI=20 gpm) averaged over 50°-70°N of UB-NAO<sup>+</sup> events during (e) 1965-1976 and (f) 2002-2013. The 80 gpm contour is marked by the green line and the thick blue line with dot denotes the zonal location of the maximum daily Z500 anomaly and its temporal variation represents the movement speed.

903  
904  
905  
906  
907  
908  
909  
910  
911  
912  
913  
914  
915  
916  
917  
918  
919  
920  
921  
922  
923  
924  
925  
926  
927  
928

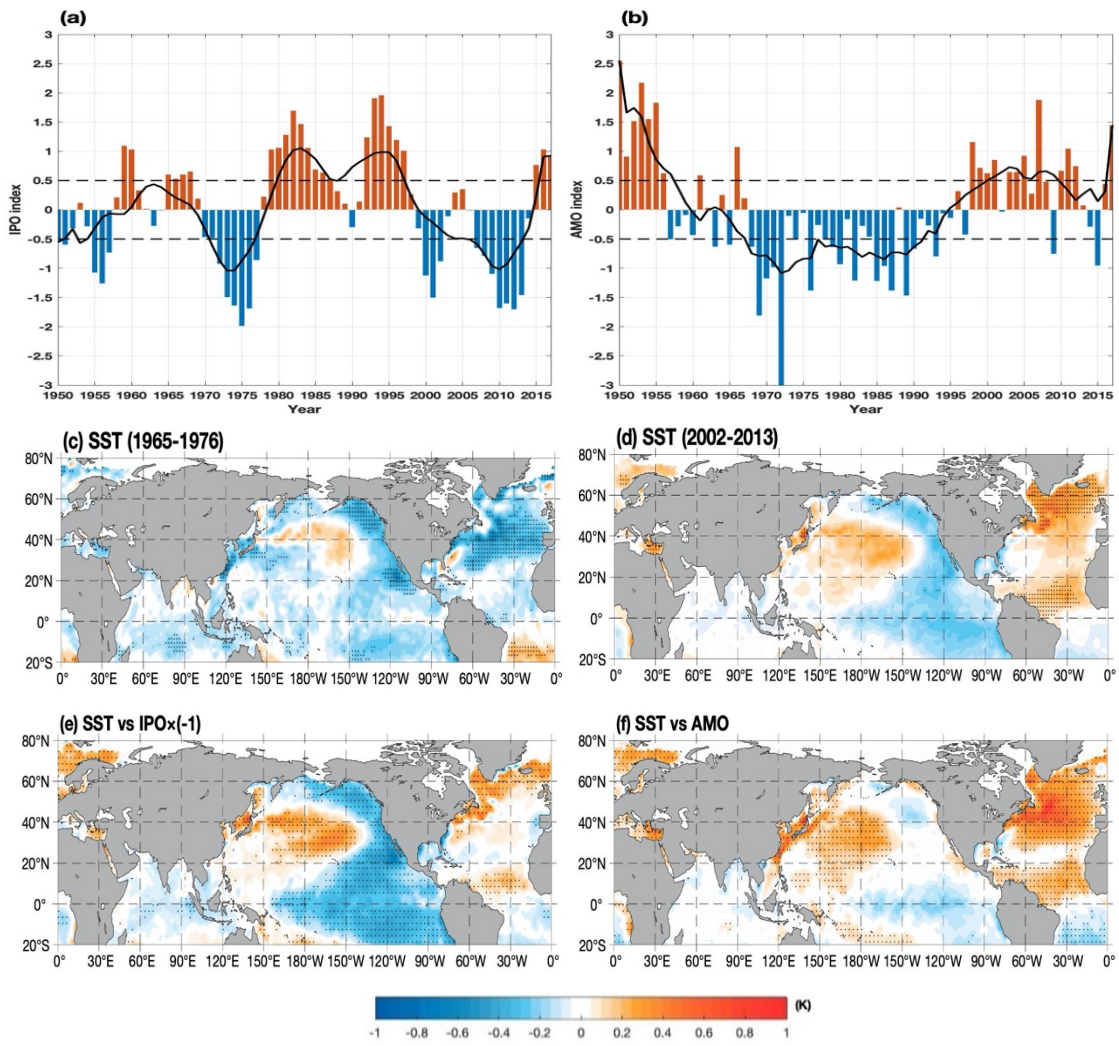
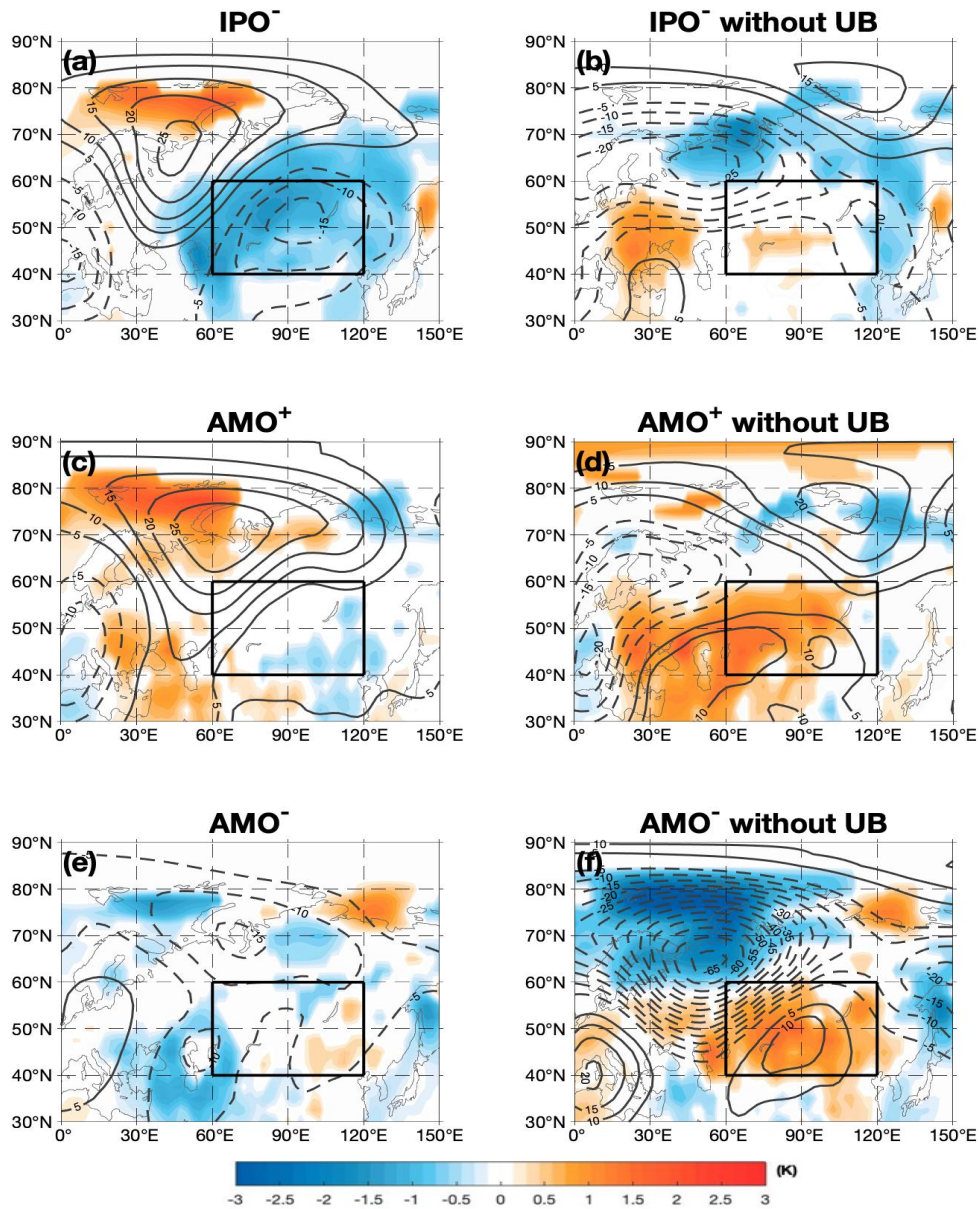


**Figure 4.** (a, b) Time series of normalized DJF-mean (a) Interdecadal Pacific Oscillation (IPO) and (b) Atlantic Multidecadal Oscillation (AMO) indices during 1950-2017, where the black solid line represents a 9-year moving average. (c, d) Time-mean winter SST anomalies during (c) 1965-1976 and (d) 2002-2013. (e, f) regressed DJF-mean SST (color shading, in K per unit index) against the normalized (a) DJF-mean IPO index (multiplied by -1.0) and (b) AMO index time series with a 9-year moving average. In panels e-f, the dot in the color shading region represents the region above the 95% confidence level based on a two-sided Student t-test.

929  
 930  
 931  
 932  
 933  
 934  
 935  
 936  
 937  
 938  
 939  
 940  
 941  
 942  
 943  
 944  
 945  
 946  
 947  
 948  
 949  
 950  
 951  
 952  
 953  
 954  
 955  
 956



957 **Figure 5.** Composite DJF-mean Z500 (contours, unit: gpm) and SAT (color shading) anomalies  
 958 in (a, b) IPO<sup>-</sup>, (c, d) AMO<sup>+</sup> and (e, f) AMO<sup>-</sup> winters during 1950-2017 based on the 0.5 STD  
 959 threshold value definition of 9-year smoothed IPO and AMO indices for days (a, c, e) with and  
 960 (b, d, f) without UB events (the case without UB represents that blocking days from lag -10 to  
 961 10 are removed for each UB event in winter). The composite field with UB events during IPO<sup>-</sup>  
 962 (AMO<sup>-</sup> or AMO<sup>+</sup>) is referred to as the IPO<sup>-</sup> (AMO<sup>-</sup> or AMO<sup>+</sup>) case, whereas the composite field  
 963 without UB events (blocking days from lag -10 to 10 days are removed) during IPO<sup>-</sup> (AMO<sup>-</sup> or  
 964 AMO<sup>+</sup>) is referred to as the IPO<sup>-</sup> (AMO<sup>-</sup> or AMO<sup>+</sup>) without UB case. Color shading represents  
 965 the areas being significant at the 95% level based on a two-sided Student t-test. Black box  
 966 represents Siberia

967  
968  
969  
970  
971  
972  
973  
974  
975  
976  
977  
978  
979  
980  
981  
982  
983  
984  
985  
986  
987  
988  
989  
990  
991  
992  
993  
994  
995  
996  
997  
998  
999  
1000  
1001  
1002  
1003  
1004  
1005  
1006

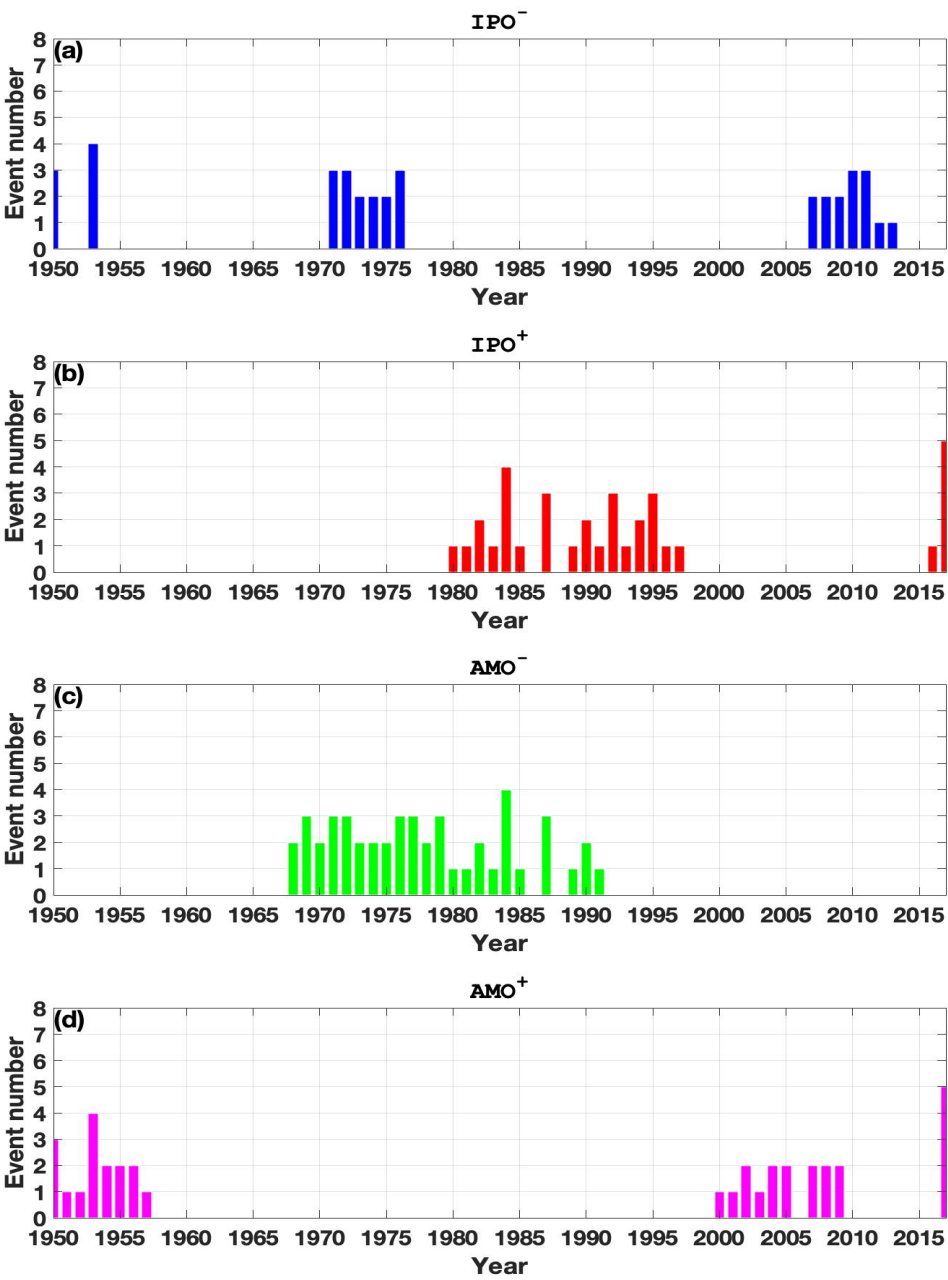
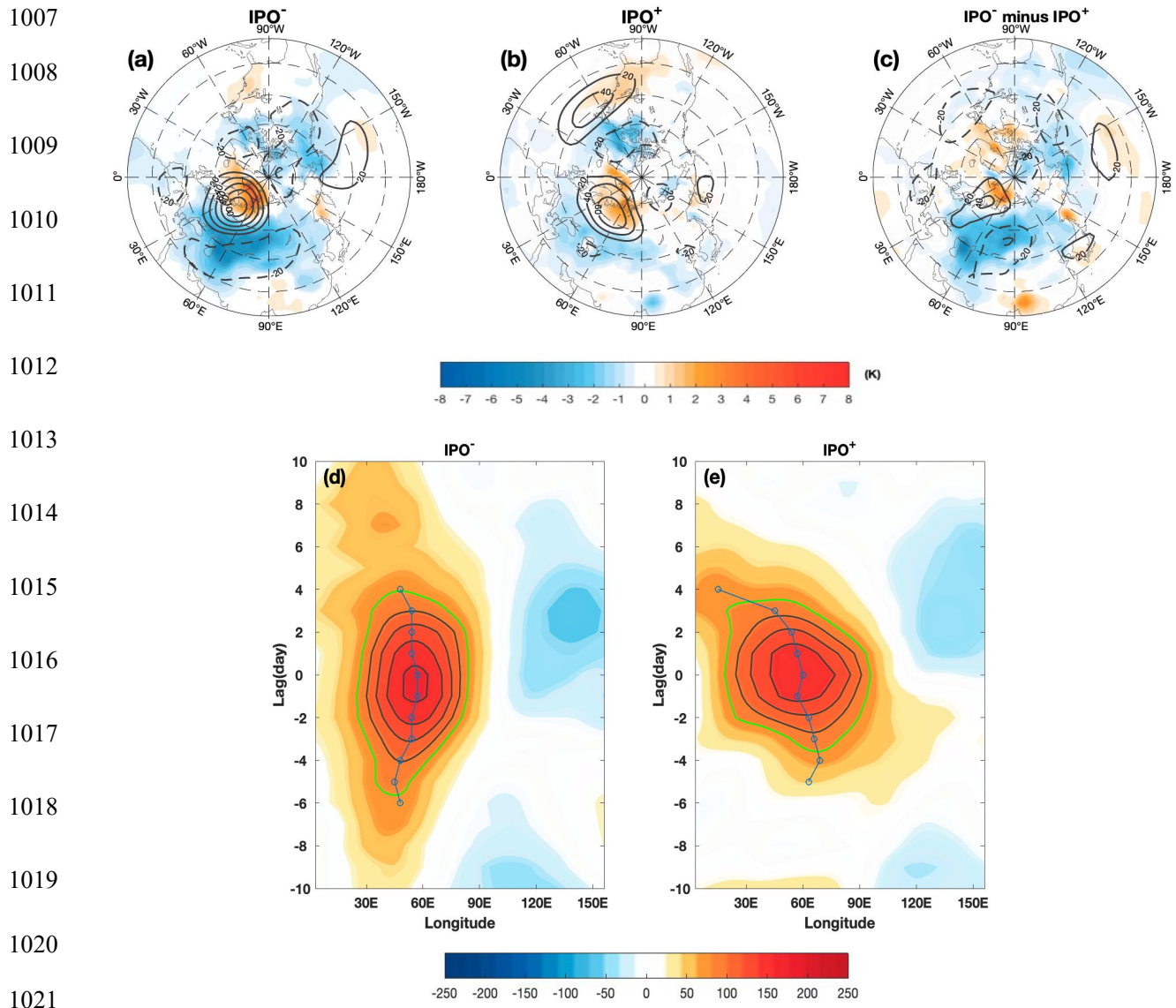
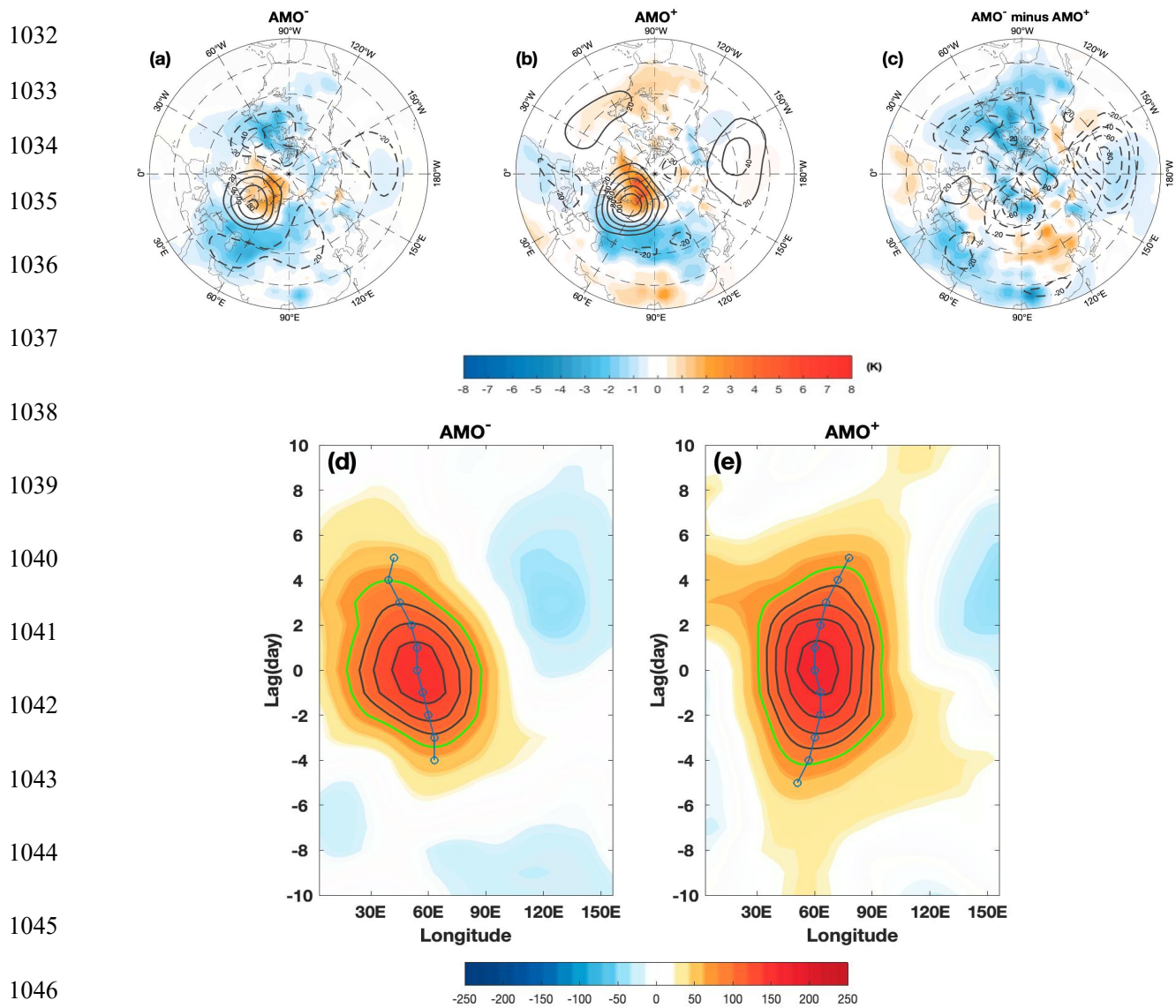


**Figure 6.** (a, b, c, d) Time series of winter UB events during (a) IPO<sup>-</sup>, (b) IPO<sup>+</sup>, (c) AMO<sup>-</sup> and (d) AMO<sup>+</sup> based on the 0.5 STD definitions of the normalized 9-year moving averaged IPO and AMO indices during 1950-2017.

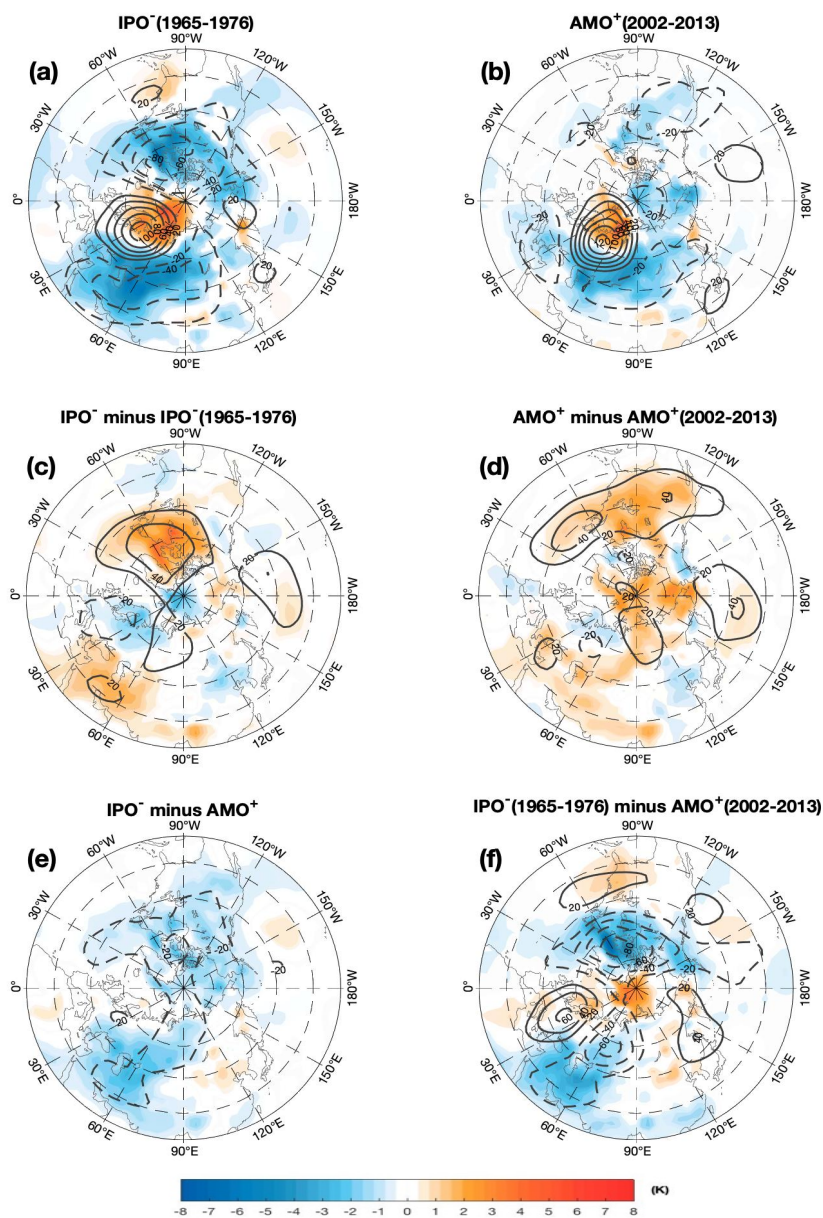


1007  
 1008  
 1009  
 1010  
 1011  
 1012  
 1013  
 1014  
 1015  
 1016  
 1017  
 1018  
 1019  
 1020  
 1021  
 1022 **Figure 7.** Time-mean composite daily Z500 (contour; CI=20 gpm) and SAT (color shading)  
 1023 anomalies averaged from lag -10 to 10 days (lag 0 denotes the peak day of blocking) of 36 UB  
 1024 events during (a) IPO<sup>-</sup> (16 cases), (b) 34 UB events during IPO<sup>+</sup> (19 cases) and (c) IPO<sup>-</sup> minus  
 1025 IPO<sup>+</sup> difference based on the 0.5 STD definition of the 9-year moving averaged IPO index. (d,  
 1026 e) time-longitude evolution of composite daily Z500 anomalies (contours; the green line  
 1027 represents 80 gpm and CI=20 gpm) averaged over the latitudes 50°-70°N of UB events during  
 1028 (d) IPO<sup>-</sup> and (e) IPO<sup>+</sup>. In panels a-b, the color shading represents the region above the 95%  
 1029 confidence level based on a two-sided Student t-test. In panels c-d, the thick blue line denotes  
 1030 the zonal location of the maximum daily Z500 anomaly and its temporal variation represents  
 1031 the movement speed.



1047 **Figure 8.** Time-mean composite daily Z500 (contours, CI=20 gpm) and SAT (color shading, in  
 1048 K) anomalies averaged from lag -10 to 10 days (lag 0 denotes the peak day of blocking) for the  
 1049 (a) 43 UB events during AMO<sup>-</sup> (22 cases), (b) 33 UB events during AMO<sup>+</sup> (18 cases) and (c)  
 1050 AMO<sup>-</sup> minus AMO<sup>+</sup> difference based on the 0.5 STD definition of the 9-year moving averaged  
 1051 AMO index from 1950-2017. (d, e) Time-longitude evolution of composite daily Z500  
 1052 anomalies (unit: gpm, the green line represents the 80 gpm contour and CI=20 gpm) averaged  
 1053 over the latitudes 50°-70°N of the UB events during (d) AMO<sup>-</sup> and (e) AMO<sup>+</sup>. In panels a-b, the  
 1054 color shading represents the region with SAT anomalies above the 95% confidence level based  
 1055 on a two-sided Student t-test. In panels d-e, the thick blue line denotes the zonal location of the  
 1056 maximum daily Z500 anomaly and its temporal variation represents the movement speed.

1057  
1058  
1059  
1060  
1061  
1062  
1063  
1064  
1065  
1066  
1067  
1068  
1069  
1070  
1071  
1072  
1073  
1074  
1075  
1076



1077 **Figure 9.** Time-mean composite daily Z500 (contours, CI=20 gpm) and SAT (color shading, in  
1078 K) anomalies averaged from lag -10 to 10 days (lag 0 denotes the peak day of blocking) of UB  
1079 events for IPO<sup>-</sup> during (a) 1965-1976 (20 UB events) and (b) AMO<sup>+</sup> during 2002-2013 (21 UB  
1080 events) as well as (c) IPO<sup>-</sup> during 1950-2017 minus IPO<sup>-</sup> (1965-1976), (d) AMO<sup>+</sup> during  
1081 1950-2017 minus AMO<sup>+</sup> (2002-2013), (e) IPO<sup>-</sup> minus AMO<sup>+</sup> during 1950-2017 and (f) IPO<sup>-</sup>  
1082 (1965-1976) minus AMO<sup>+</sup> (2002-2013) differences based on 9-year smoothed IPO and AMO  
1083 indices. The color shading represents the region above the 95% confidence level based on a  
1084 two-sided Student t-test.

1085  
 1086  
 1087  
 1088  
 1089  
 1090  
 1091  
 1092  
 1093  
 1094  
 1095  
 1096  
 1097  
 1098  
 1099  
 1100  
 1101  
 1102  
 1103  
 1104  
 1105  
 1106  
 1107  
 1108  
 1109  
 1110  
 1111  
 1112  
 1113

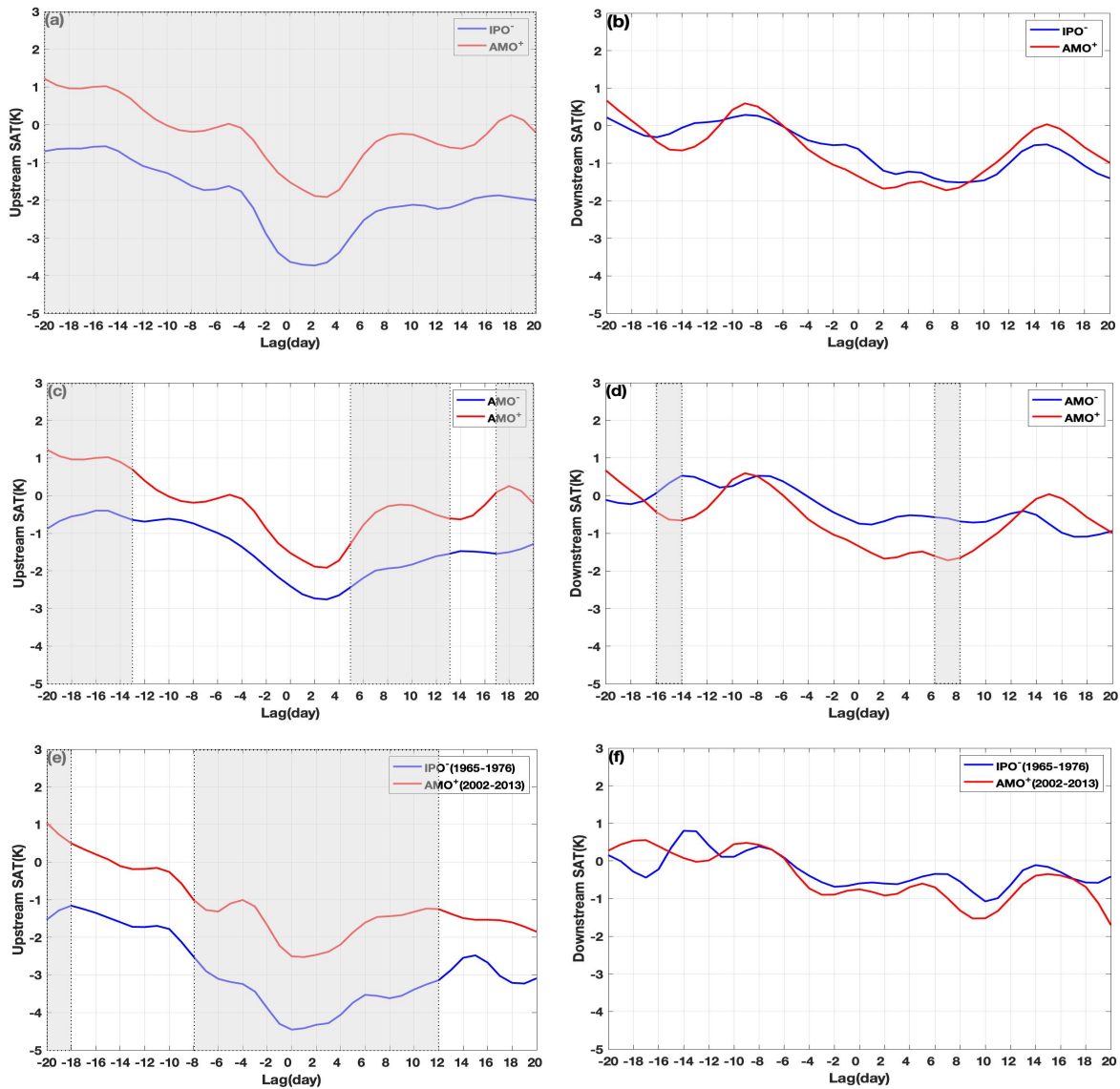


**Figure 10.** Time evolution of composite daily SAT anomalies averaged over (a, c, e) upstream (30°-50°N, 30°-70°E) and (b, d, f) downstream (30°-50°N, 90°-130°E) regions, referred to as upstream and downstream SAT anomalies, during the UB life cycle from lag -20 to 20 days (lag 0 denotes the peak day) for UB events during IPO<sup>-</sup> (blue line), AMO<sup>-</sup> (blue line) and AMO<sup>+</sup> (red line) during (a, b, c, d)1950-2018 and (e, f) 1965-1976 and 2002-2013. The gray shading represents the difference of two curves being significant at the 95% confidence level for a Monte-Carlo test based on a 5000 times simulation.

1114  
 1115  
 1116  
 1117  
 1118  
 1119  
 1120  
 1121  
 1122  
 1123  
 1124  
 1125  
 1126  
 1127  
 1128  
 1129  
 1130  
 1131  
 1132  
 1133  
 1134  
 1135  
 1136  
 1137  
 1138  
 1139  
 1140  
 1141  
 1142  
 1143  
 1144  
 1145

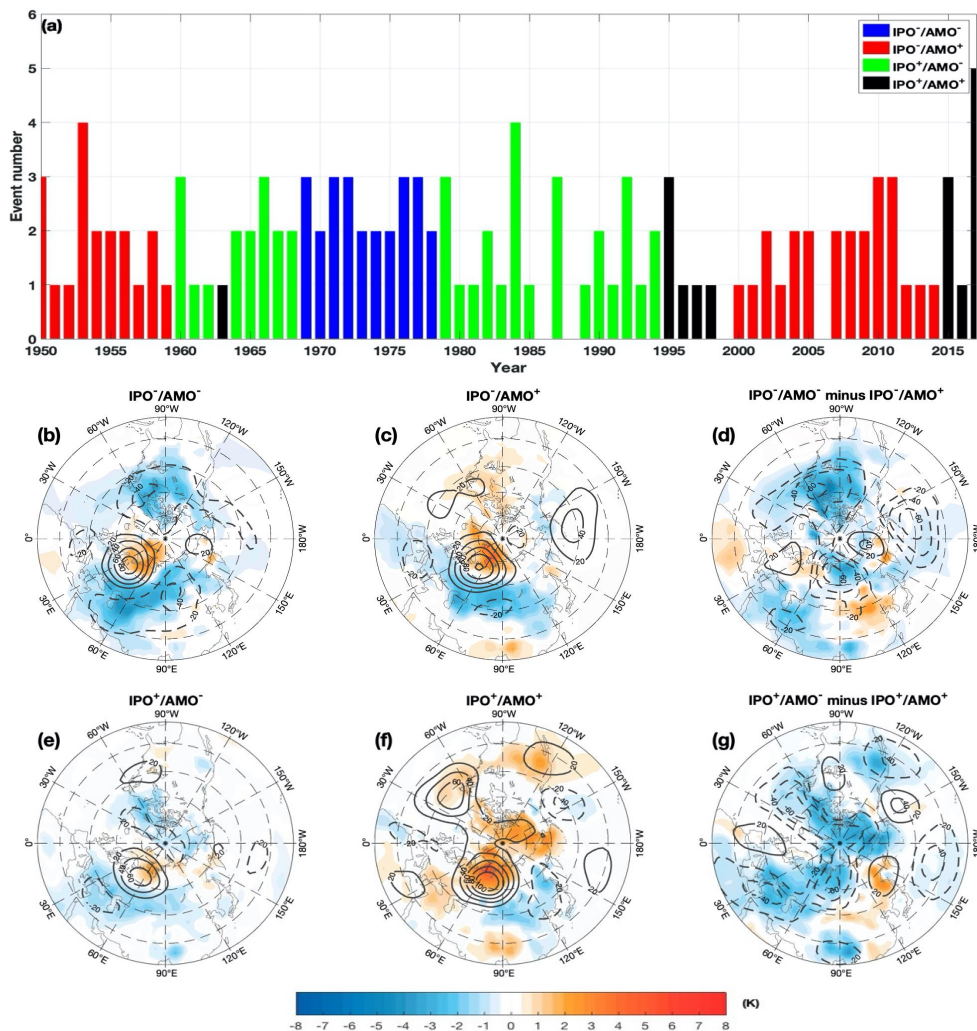
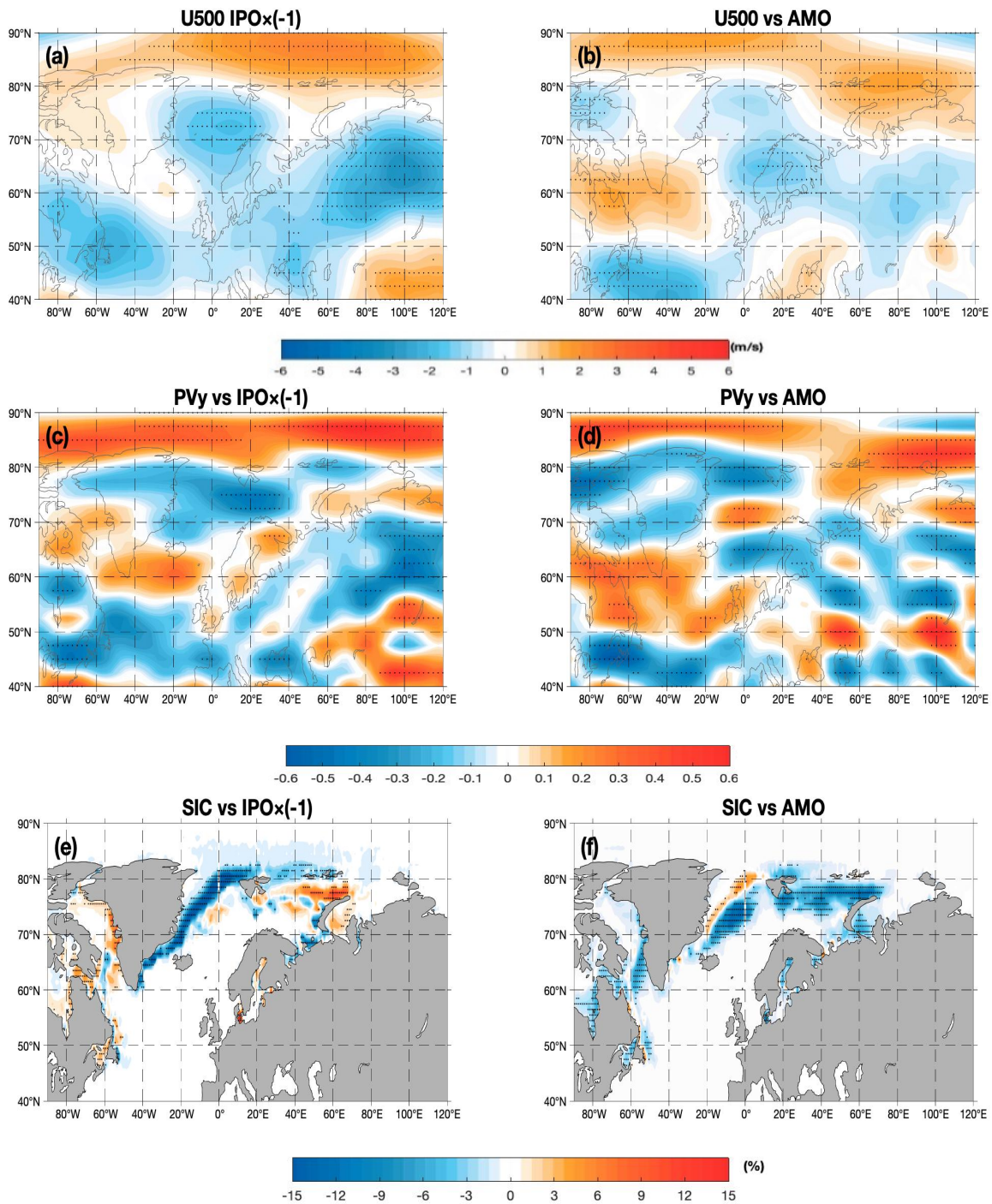


**Figure 11.** (a) Time series of winter UB events in winter for IPO<sup>-</sup> /AMO<sup>-</sup> (10 cases, blue), IPO<sup>-</sup>/AMO<sup>+</sup> (24 cases, red), IPO<sup>+</sup>/AMO<sup>-</sup> (22 cases, green), and (black) IPO<sup>+</sup>/AMO<sup>+</sup> (8 cases, black) combinations based on 9-year smoothed IPO and AMO indices. (b, c, d, e) Time-mean Z500 (contour, CI=20 gpm) and SAT (color shading) anomalies averaged from lag -10 to 10 days (lag 0 denotes the peak day of blocking) of 25, 43, 42 and 16 UB events during (b) IPO<sup>-</sup>/AMO<sup>-</sup>, (c) IPO<sup>-</sup>/AMO<sup>+</sup>, (d) IPO<sup>+</sup>/AMO<sup>-</sup>, and (e) IPO<sup>+</sup>/AMO<sup>+</sup> combinations. In panels b-e, the color shading represents the region above the 95% confidence level based on a two-sided Student t-test.

1146  
 1147  
 1148  
 1149  
 1150  
 1151  
 1152  
 1153  
 1154  
 1155  
 1156  
 1157  
 1158  
 1159  
 1160  
 1161  
 1162  
 1163  
 1164



1165 **Figure 12.** DJF-mean (a, b) U500, (c, d) non-dimensional  $PV_y$  for UB events removed and (e, f)  
 1166 SIC anomalies regressed onto the time series of normalized DJF-mean (a, c, e) IPO index  
 1167 (multiplied by -1.0) and (b, d, f) AMO index with a 9-year smoothing. The dot represents the  
 1168 region above the 95% confidence level for a two-sided Student t-test.

# Figures

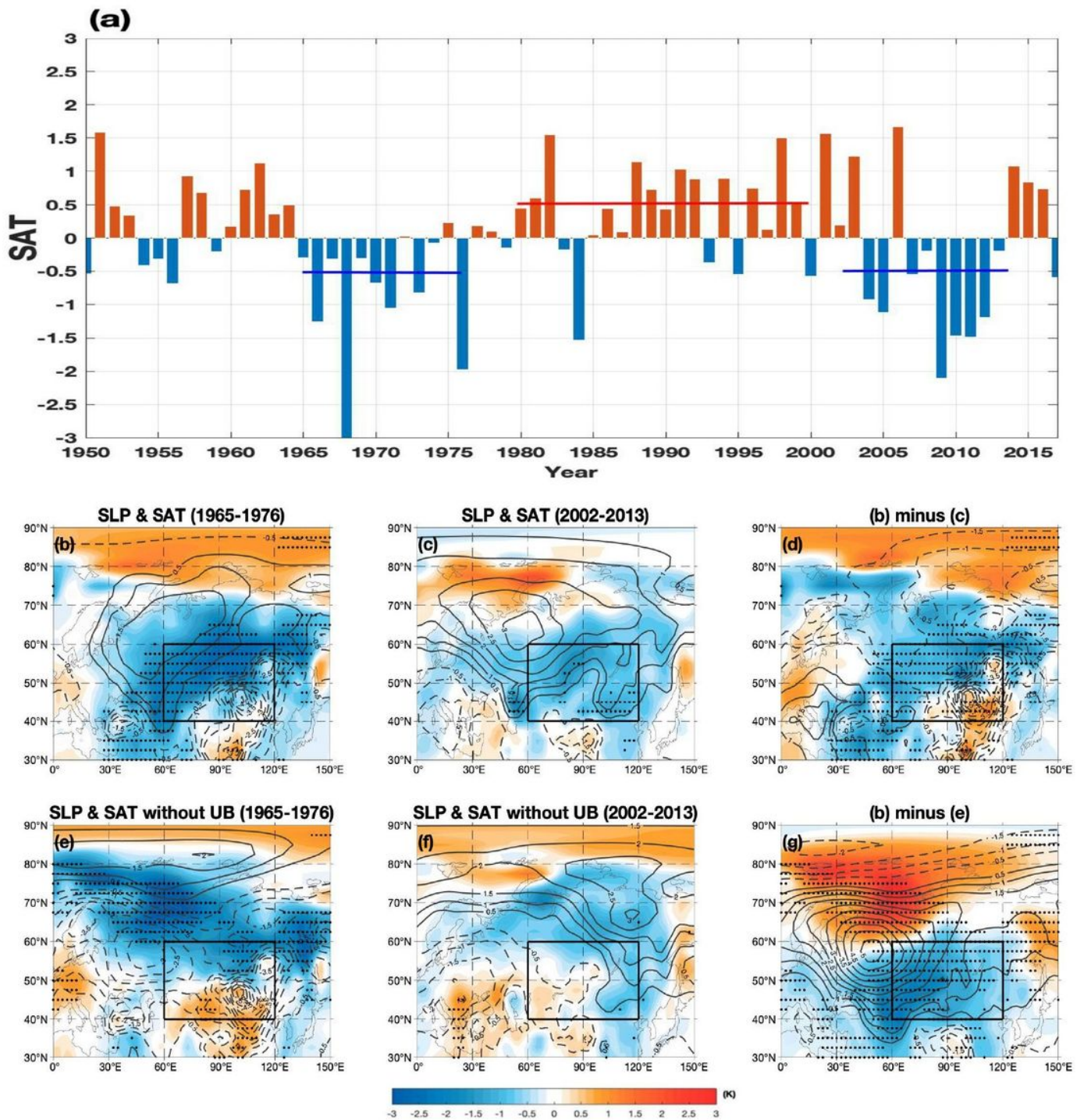


**Figure 1**

(a) Time series of DJF-mean surface air temperature (SAT) anomalies averaged over central Eurasia (60°-120°E, 40°-60°N), with the red line denoting the 1980-2000 period, and the blue line marking the 1965-1976 and 2002-2013 periods. (b, c, d, e, f, g) DJF-mean sea surface pressure (SLP) (contours; contour interval (CI)=0.5 hPa) and SAT (color shading in K) anomalies averaged during (b, e) 1965-1976

and (c, f) 2002-2013 for UB events (b, c) included and (e, f) excluded (blocking days from lag -10 to 10 days are excluded, lag 0 denotes the day of the UB peak) as well as (d) b minus c and (g) b minus e differences. The dot represents the areas of the SAT anomaly being significant at the 95% level based on a two-sided Student t-test. Black box represents central Eurasia.

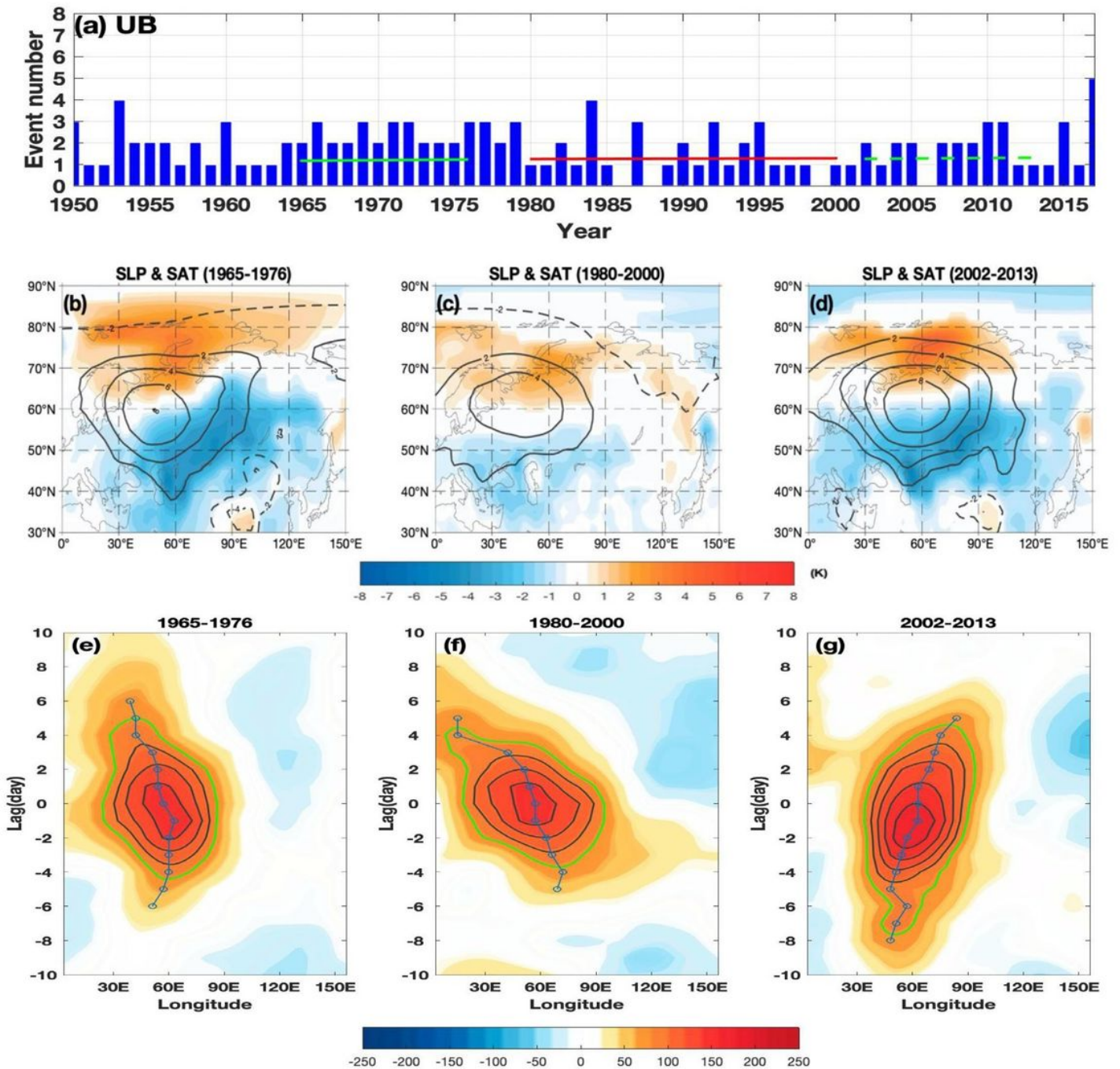


**Figure 2**

(a) Time series of the number of winter Ural blocking (UB) events (a total of 126 cases) during 1950-2017 with three sub-periods: 1965-1976 (29 cases, blue line), 1980-2000 (30 cases; red line) and 2002-2013 (21 cases; dashed green line). (b, c, d) Time-mean composite daily SLP (contours, CI=2 hPa) and SAT (color

shading, in K) anomalies averaged from lag -10 to 10 days (lag 0 denotes the peak day of blocking) for (b) 29 UB events during 1965-1976, (c) 30 UB events during 1980-2000 and (d) 21 UB events during 2002-2013. (e, f, g) Time-longitude evolution of the composite daily Z500 anomalies (unit: gpm and CI=20 gpm) averaged over 50o-70oN of the UB events during (e) 1965-1976, (f) 1980-2000 and (g) 2002-2013. In (e-g), the 80 gpm contour is marked by the green line and the thick blue line denotes the zonal location of the maximum daily Z500 anomaly whose temporal variation represents the movement speed. The color shading represents the region above the 95% confidence level based on a two-sided Student t-test.

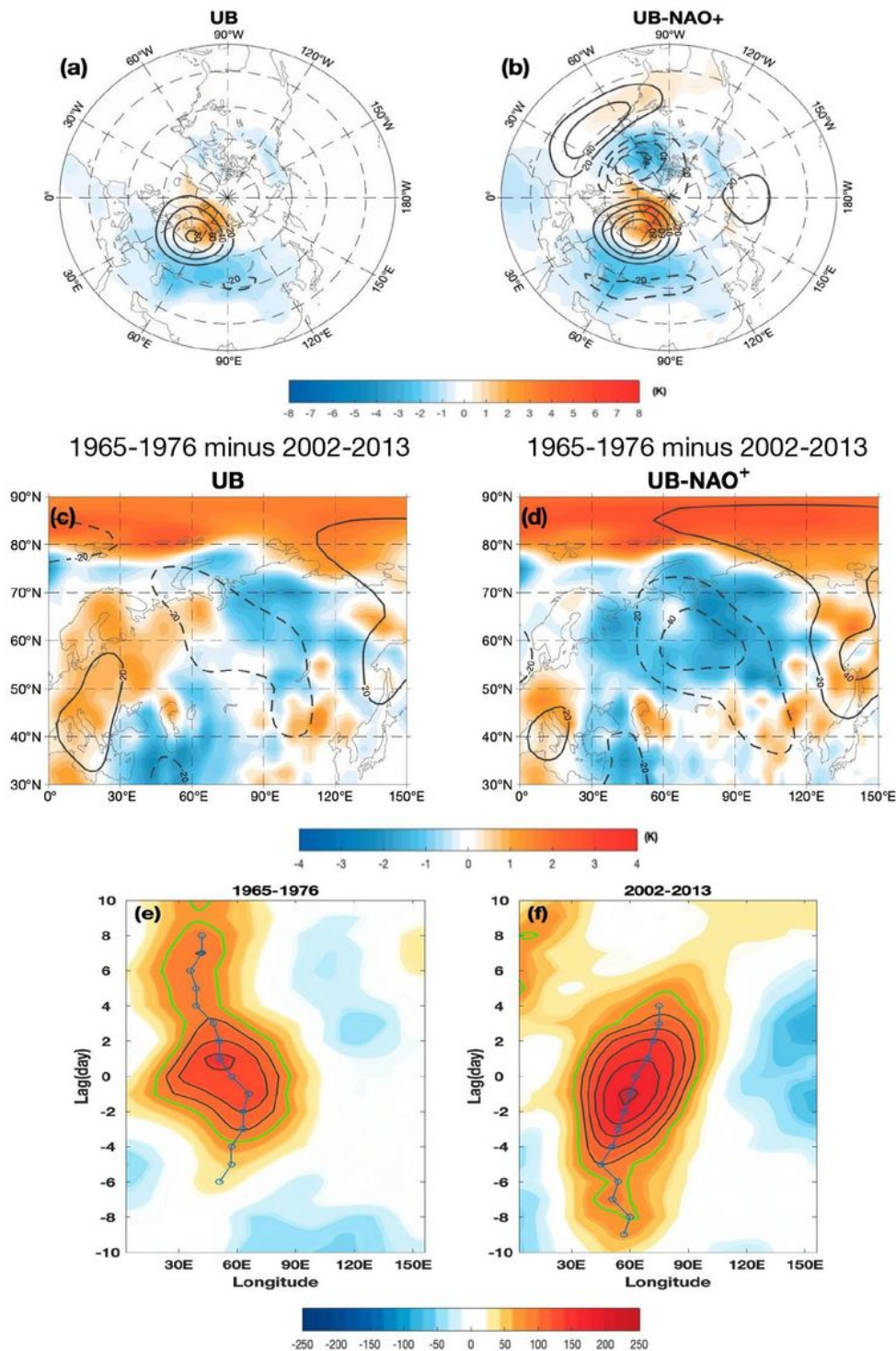


**Figure 3**

Time-mean composite daily 500-hPa geopotential height (Z500) (contours, CI=20 gpm) and SAT (color shading, unit: K) anomalies averaged from lag -10 to 10 days (lag 0 denotes the peak day of blocking) for (a) UB and (b) UB-NAO+ events during 1950-2017. (c, d) 1965-1976 minus 2002-2013 differences of time-mean Z500 and SAT anomalies for (c) UB and (d) UB-NAO+ events, where the color shading represents the region above the 95% confidence level based on a two-sided Student t-test. (e, f) Time-longitude evolution of composite daily Z500 anomalies (unit: gpm and CI=20 gpm) averaged over 50o-70oN of UB-NAO+ events during (e) 1965-1976 and (f) 2002-2013. The 80 gpm contour is marked by the green line and the thick blue line with dot denotes the zonal location of the maximum daily Z500 anomaly and its temporal variation represents the movement speed.

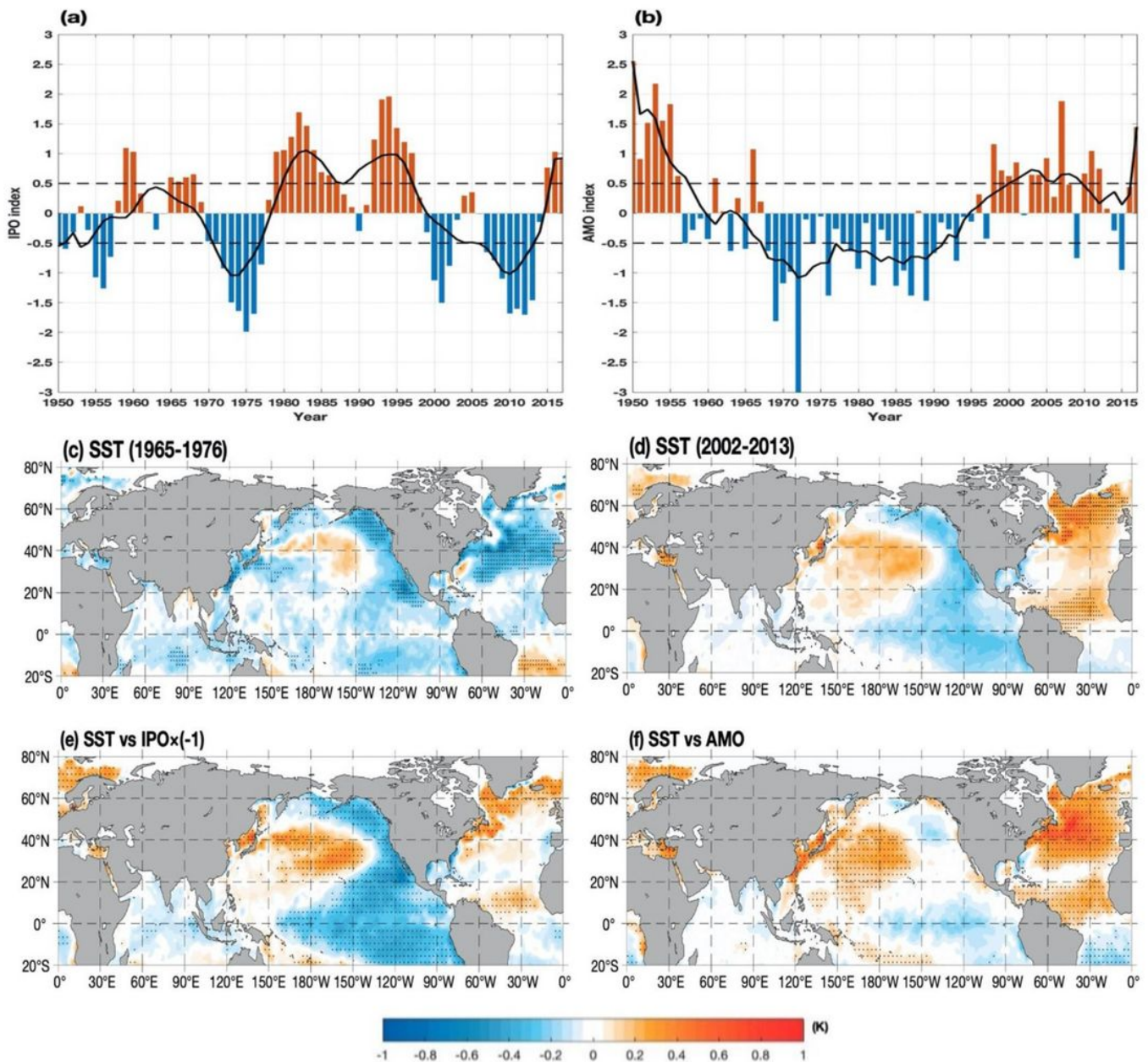


## Figure 4

(a, b) Time series of normalized DJF-mean (a) Interdecadal Pacific Oscillation (IPO) and (b) Atlantic Multidecadal Oscillation (AMO) indices during 1950-2017, where the black solid line represents a 9-year moving average. (c, d) Time-mean winter SST anomalies during (c) 1965-1976 and (d) 2002-2013. (e, f) regressed DJF-mean SST (color shading, in K per unit index) against the normalized (a) DJF-mean IPO index (multiplied by -1.0) and (b) AMO index time series with a 9-year moving average. In panels e-f, the dot in the color shading region represents the region above the 95% confidence level based on a two-sided Student t-test. Note: The designations employed and the presentation of the material on this map do not imply the expression of any opinion whatsoever on the part of Research Square concerning the legal status of any country, territory, city or area or of its authorities, or concerning the delimitation of its frontiers or boundaries. This map has been provided by the authors.

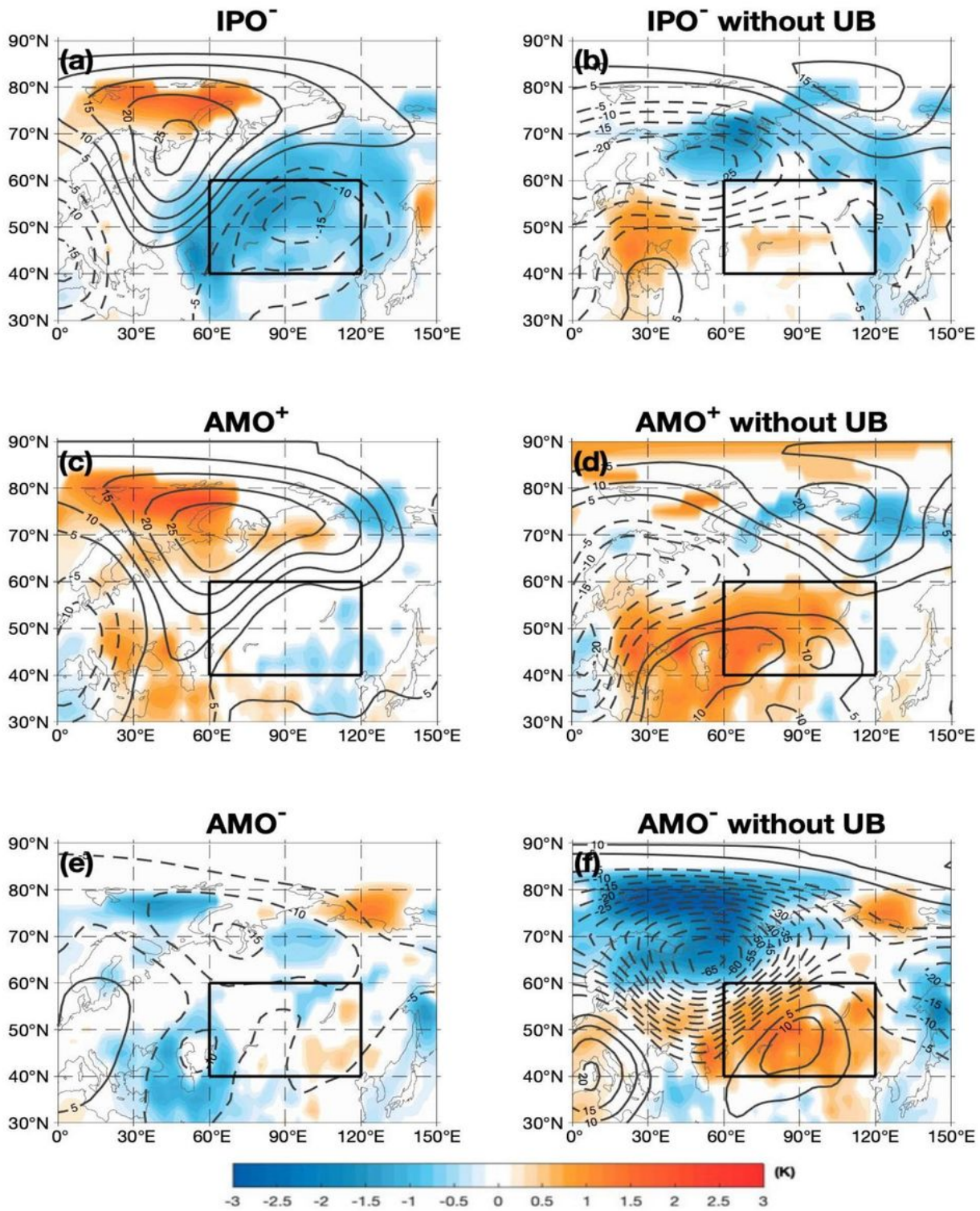


**Figure 5**

Composite DJF-mean Z500 (contours, unit: gpm) and SAT (color shading) anomalies in (a, b) IPO-, (c, d) AMO+ and (e, f) AMO- winters during 1950-2017 based on the 0.5 STD threshold value definition of 9-year smoothed IPO and AMO indices for days (a, c, e) with and (b, d, f) without UB events (the case without UB represents that blocking days from lag -10 to 10 are removed for each UB event in winter). The composite field with UB events during IPO- (AMO- or AMO+) is referred to as the IPO- (AMO- or AMO+) case, whereas

the composite field without UB events (blocking days from lag -10 to 10 days are removed) during IPO- (AMO- or AMO+) is referred to as the IPO- (AMO- or AMO+) without UB case. Color shading represents the areas being significant at the 95% level based on a two-sided Student t-test. Black box represents Siberia

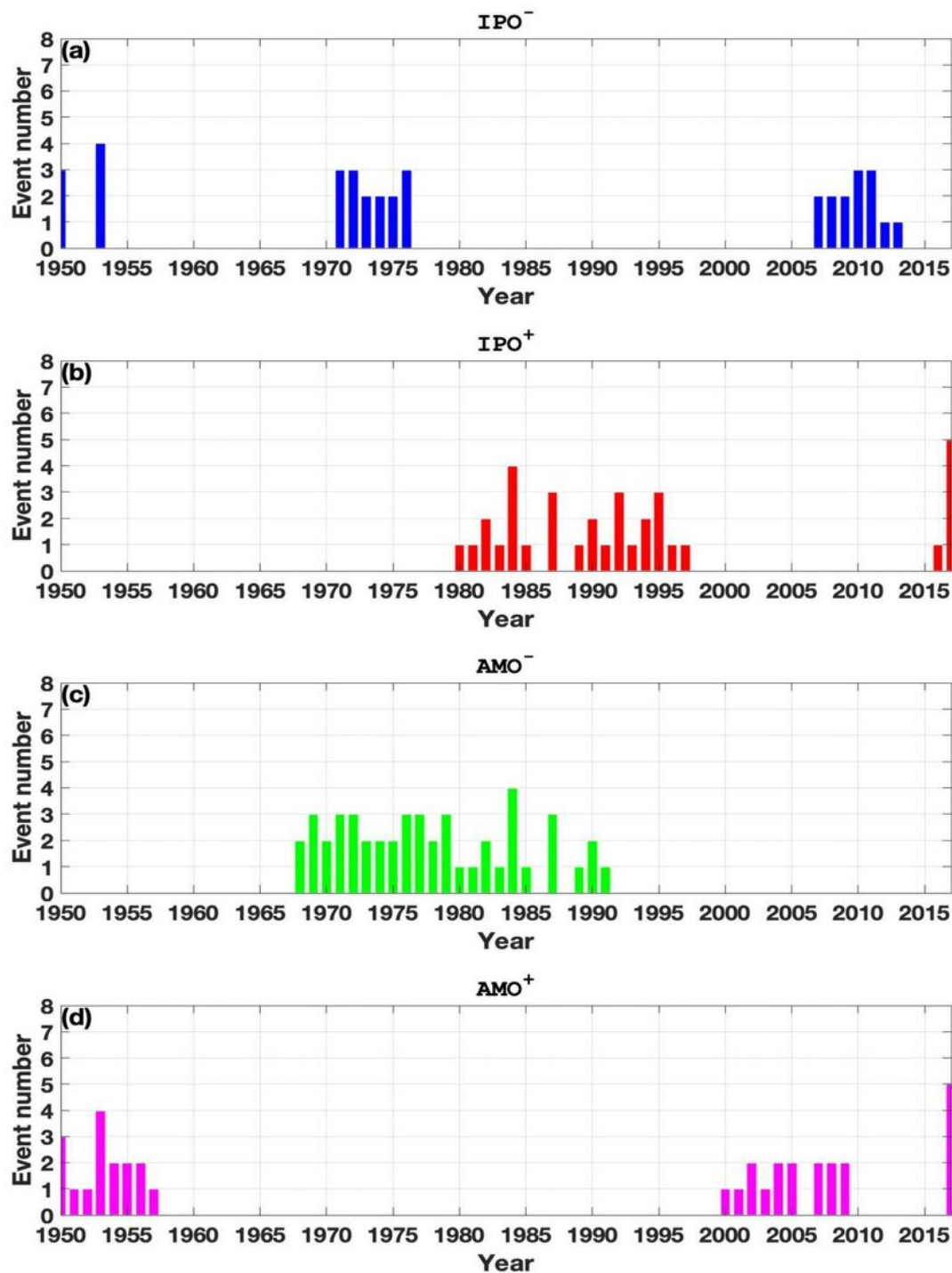
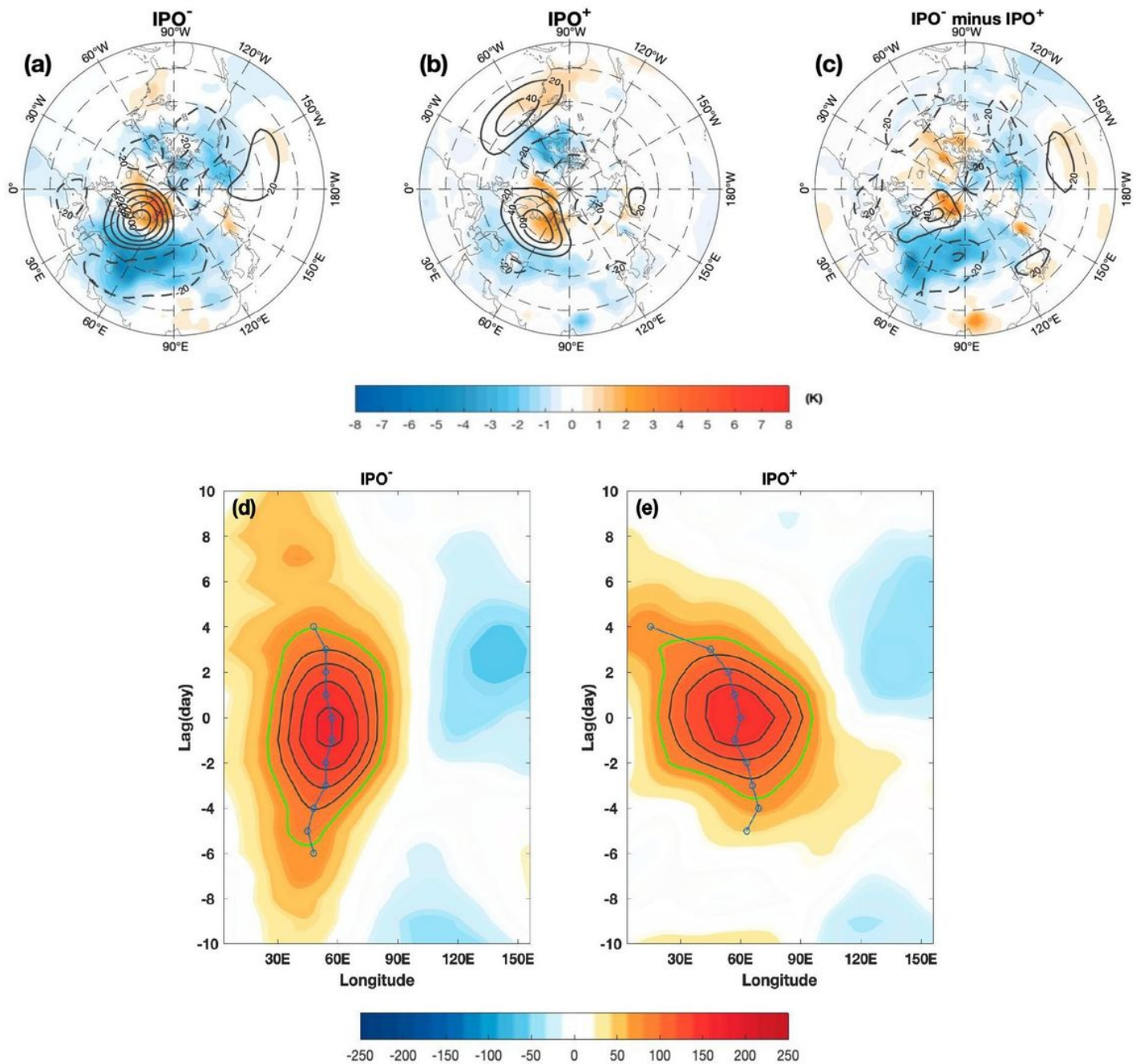


Figure 6

(a, b, c, d) Time series of winter UB events during (a) IPO-, (b) IPO+, (c) AMO- and (d) AMO+ based on the 0.5 STD definitions of the normalized 9-year moving averaged IPO and AMO indices during 1950-2017.



**Figure 7**

Time-mean composite daily Z500 (contour; CI=20 gpm) and SAT (color shading) anomalies averaged from lag -10 to 10 days (lag 0 denotes the peak day of blocking) of 36 UB events during (a) IPO- (16 cases), (b) 34 UB events during IPO+ (19 cases) and (c) IPO- minus IPO+ difference based on the 0.5 STD definition of the 9-year moving averaged IPO index. (d, e) time-longitude evolution of composite daily Z500 anomalies (contours; the green line represents 80 gpm and CI=20 gpm) averaged over the latitudes 50o-70oN of UB events during (d) IPO- and (e) IPO+. In panels a-b, the color shading represents the region above the 95% confidence level based on a two-sided Student t-test. In panels c-d, the thick blue line

denotes the zonal location of the maximum daily Z500 anomaly and its temporal variation represents the movement speed.

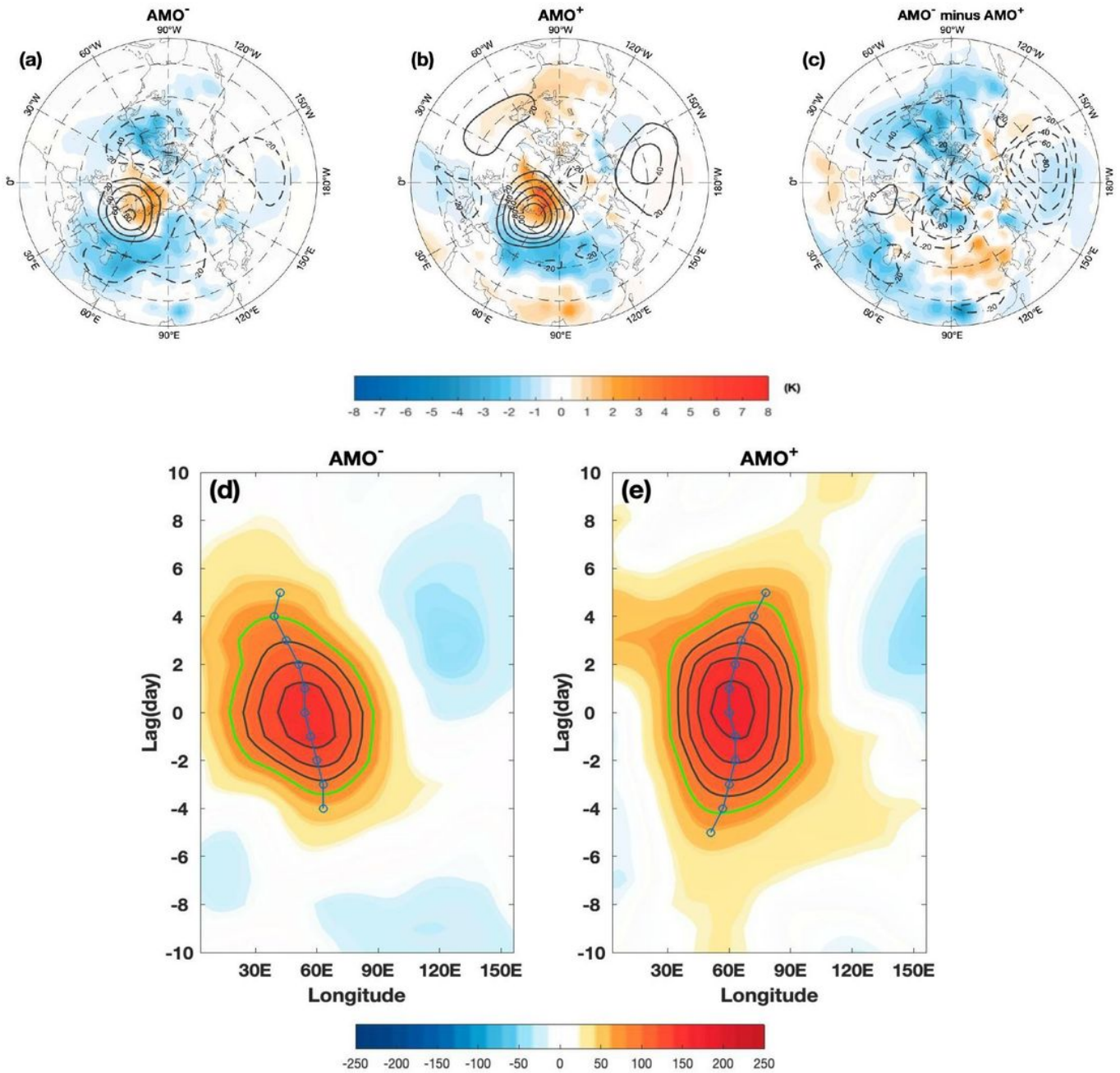


**Figure 8**

Time-mean composite daily Z500 (contours, CI=20 gpm) and SAT (color shading, in K) anomalies averaged from lag -10 to 10 days (lag 0 denotes the peak day of blocking) for the (a) 43 UB events during AMO<sup>-</sup> (22 cases), (b) 33 UB events during AMO<sup>+</sup> (18 cases) and (c) AMO<sup>-</sup> minus AMO<sup>+</sup> difference based on the 0.5 STD definition of the 9-year moving averaged AMO index from 1950-2017. (d, e) Time-longitude evolution of composite daily Z500 anomalies (unit: gpm, the green line represents the 80 gpm

contour and CI=20 gpm) averaged over the latitudes 50o-70oN of the UB events during (d) AMO- and (e) AMO+. In panels a-b, the color shading represents the region with SAT anomalies above the 95% confidence level based on a two-sided Student t-test. In panels d-e, the thick blue line denotes the zonal location of the maximum daily Z500 anomaly and its temporal variation represents the movement speed.

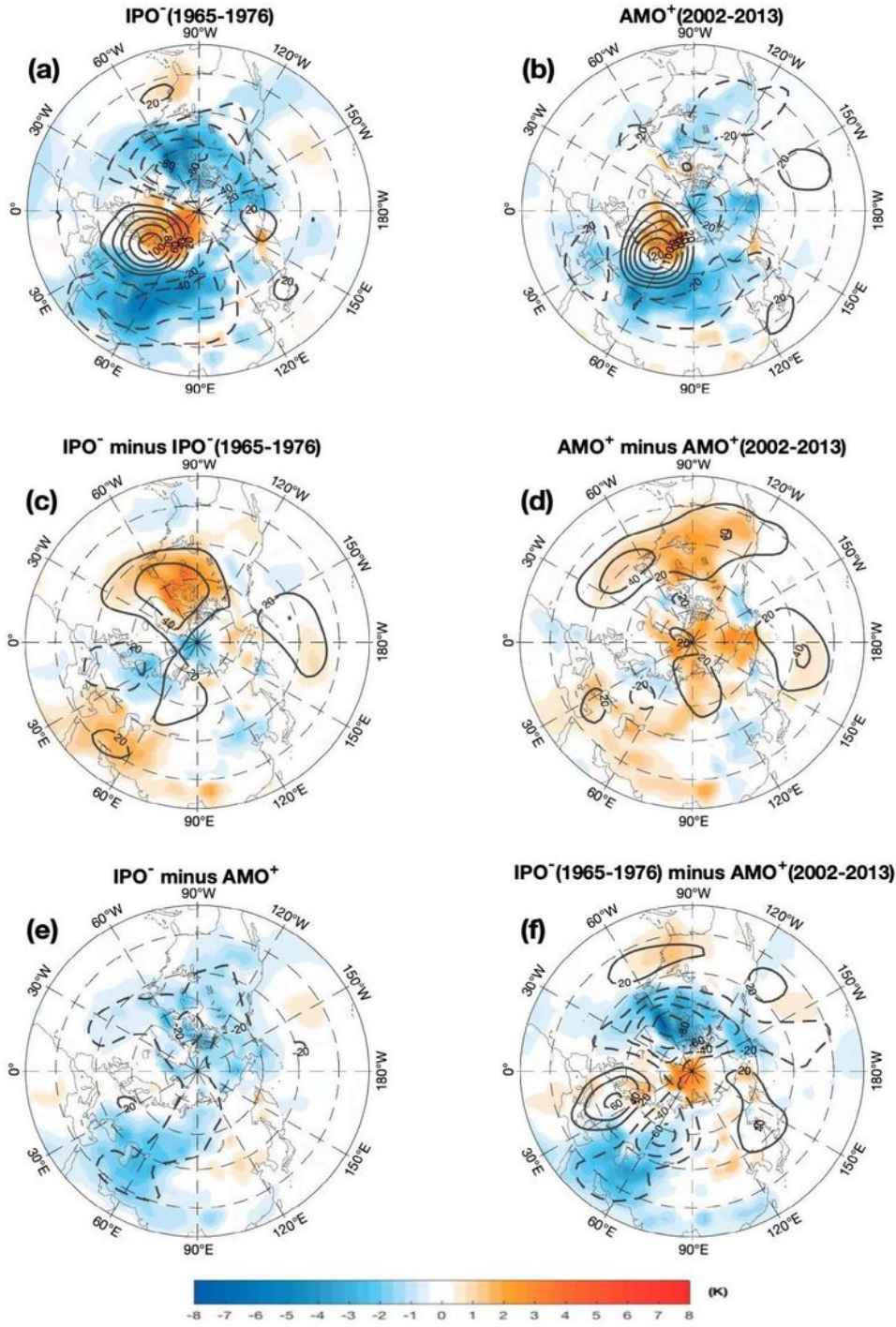


Figure 9

Time-mean composite daily Z500 (contours, CI=20 gpm) and SAT (color shading, in K) anomalies averaged from lag -10 to 10 days (lag 0 denotes the peak day of blocking) of UB events for IPO- during (a) 1965-1976 (20 UB events) and (b) AMO+ during 2002-2013 (21 UB events) as well as (c) IPO- during 1950-2017 minus IPO- (1965-1976), (d) AMO+ during 1950-2017 minus AMO+ (2002-2013), (e) IPO- minus AMO+ during 1950-2017 and (f) IPO- (1965-1976) minus AMO+ (2002-2013) differences based on 9-year smoothed IPO and AMO indices. The color shading represents the region above the 95% confidence level based on a two-sided Student t-test.

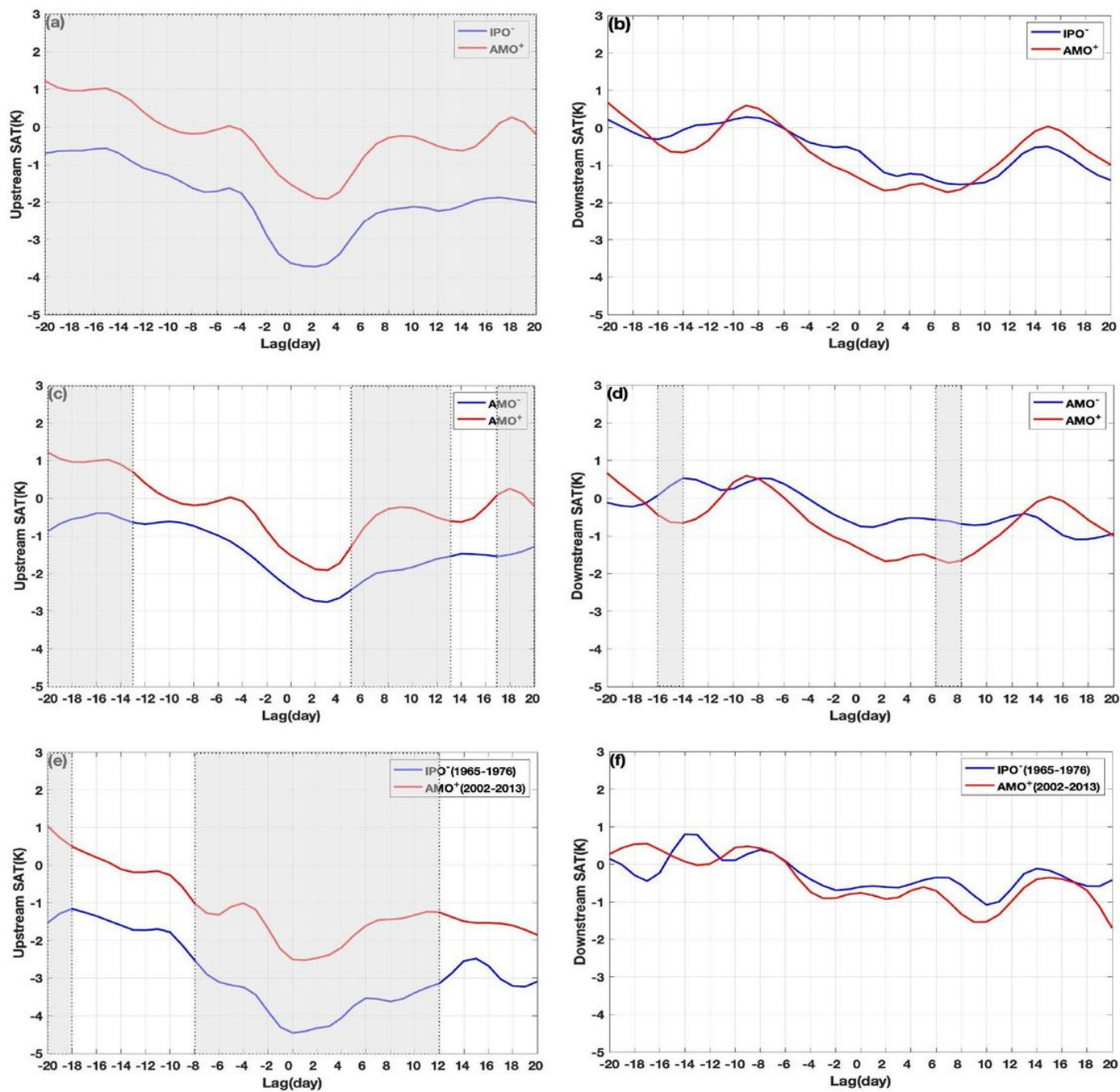


Figure 10

Time evolution of composite daily SAT anomalies averaged over (a, c, e) upstream (30o-50oN, 30o-70oE) and (b, d, f) downstream (30o-50oN, 90o-130oE) regions, referred to as upstream and downstream SAT anomalies, during the UB life cycle from lag -20 to 20 days (lag 0 denotes the peak day) for UB events during IPO- (blue line), AMO- (blue line) and AMO+ (red line) during (a, b, c, d) 1950-2018 and (e, f) 1965-1976 and 2002-2013. The gray shading represents the difference of two curves being significant at the 95% confidence level for a Monte-Carlo test based on a 5000 times simulation.

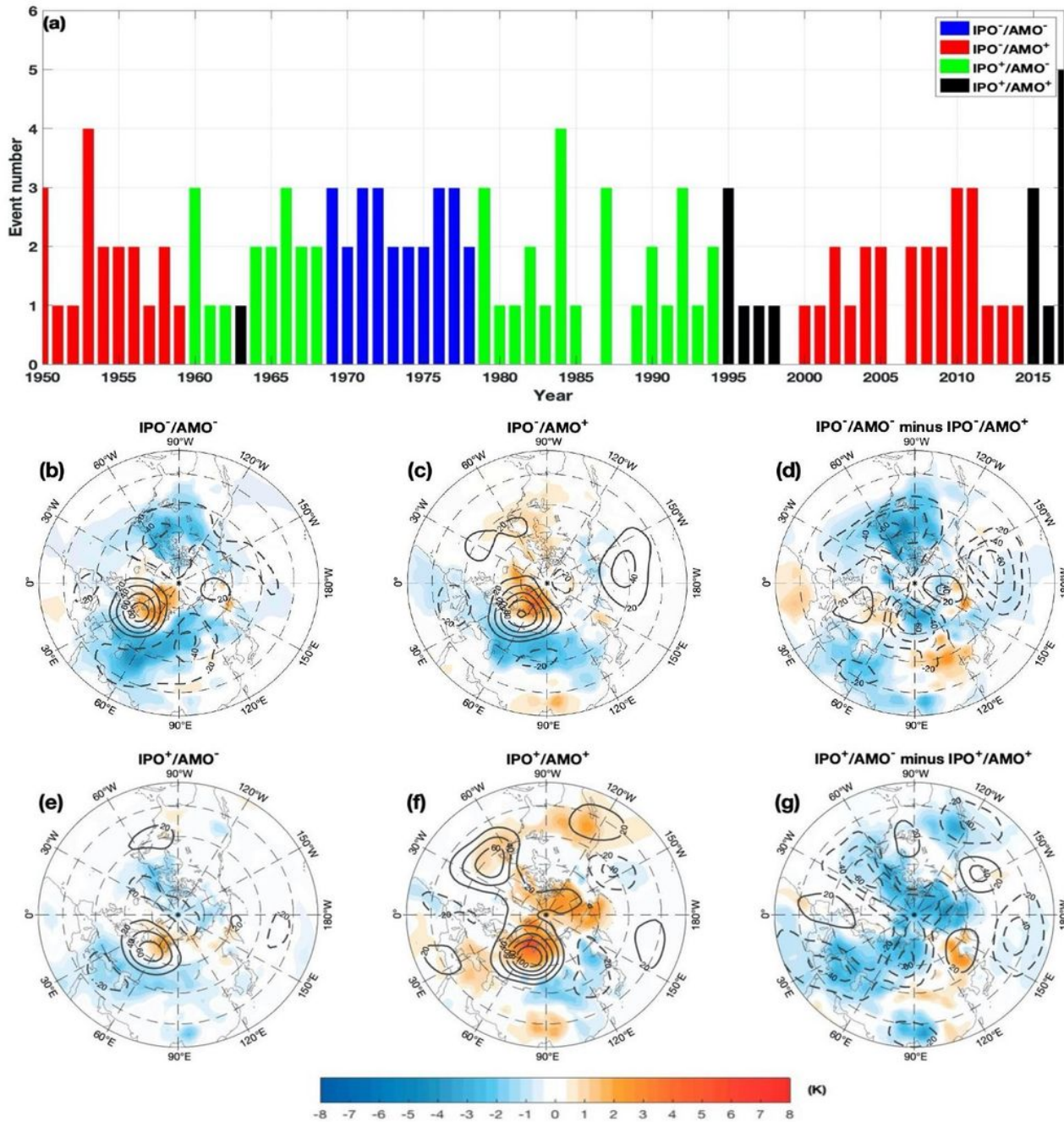
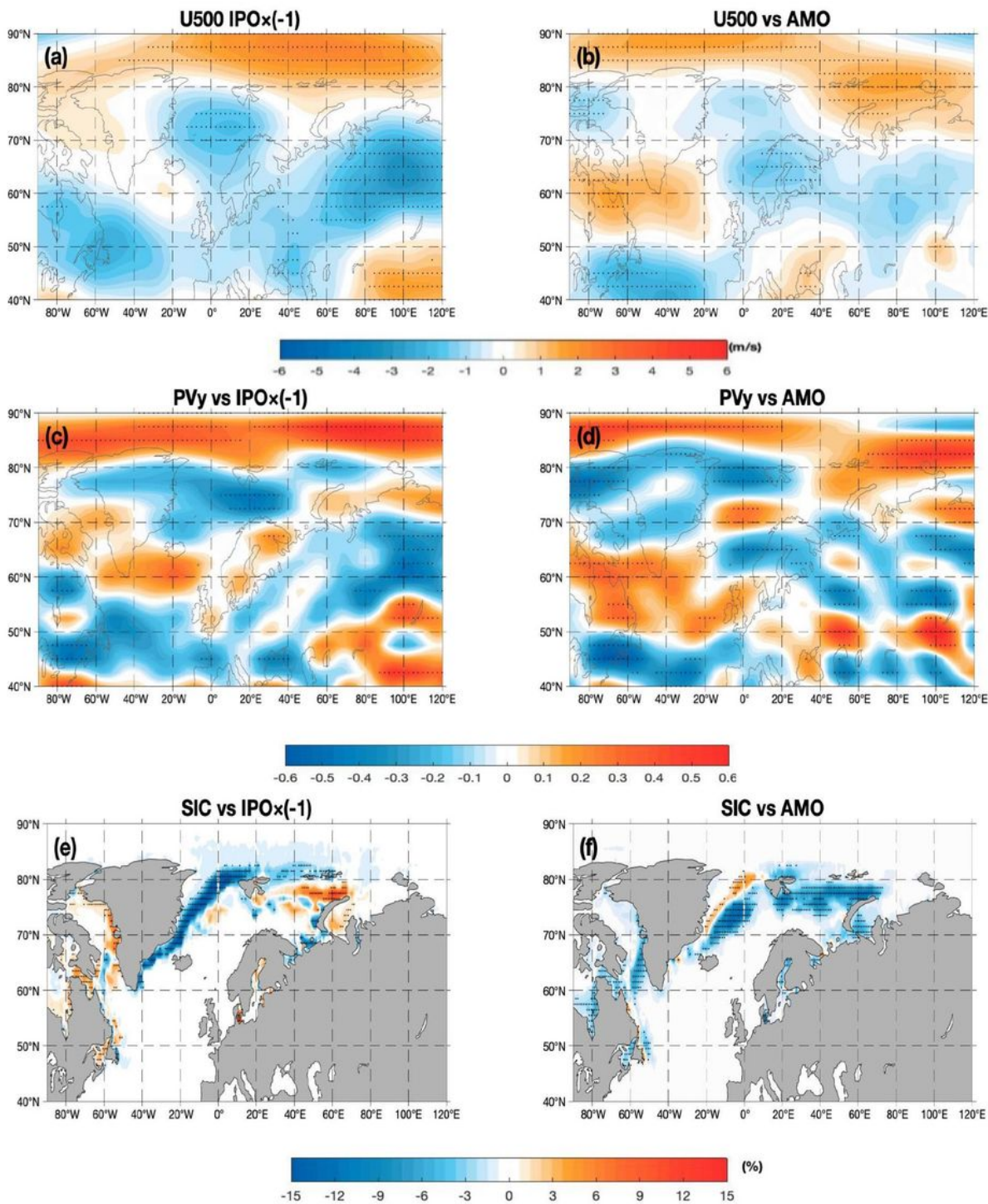


Figure 11

(a) Time series of winter UB events in winter for IPO- /AMO- (10 cases, blue), IPO-/AMO+ (24 cases, red), IPO+/AMO- (22 cases, green), and (black) IPO+/AMO+ (8 cases, black) combinations based on 9-year smoothed IPO and AMO indices. (b, c, d, e) Time-mean Z500 (contour, CI=20 gpm) and SAT (color shading) anomalies averaged from lag -10 to 10 days (lag 0 denotes the peak day of blocking) of 25, 43, 42 and 16 UB events during (b) IPO-/AMO-, (c) IPO-/AMO+, (d) IPO+/AMO-, and (e) IPO+/AMO+ combinations. In panels b-e, the color shading represents the region above the 95% confidence level based on a two-sided Student t-test.



## Figure 12

DJF-mean (a, b) U500, (c, d) non-dimensional PVy for UB events removed and (e, f) SIC anomalies regressed onto the time series of normalized DJF-mean (a, c, e) IPO index (multiplied by -1.0) and (b, d, f) AMO index with a 9-year smoothing. The dot represents the region above the 95% confidence level for a two-sided Student t-test.

## Supplementary Files

This is a list of supplementary files associated with this preprint. Click to download.

- [Supplementaryfile416.pdf](#)